2018

Optically controlled laser–plasma electron accelerator for compact gamma-ray sources

S. Y. Kalmykov

X. Davoine

I. Ghebregziabher

B. A. Shadwick

PAPER • OPEN ACCESS

Optically controlled laser–plasma electron accelerator for compact gamma-ray sources

To cite this article: S Y Kalmykov *et al* 2018 *New J. Phys.* **20** 023047

New Journal of Physics
The open access journal at the forefront of physics

Deutsche Physikalische Gesellschaft DPG
IOP Institute of Physics

Published in partnership with: Deutsche Physikalische Gesellschaft and the Institute of Physics

OPEN ACCESS

RECEIVED
15 August 2017

REVISED
1 December 2017

ACCEPTED FOR PUBLICATION
6 February 2018

PUBLISHED
22 February 2018

PAPER

Optically controlled laser–plasma electron accelerator for compact gamma-ray sources

S Y Kalmykov[1,4], X Davoine[2], I Ghebregziabher[3] and B A Shadwick[1]

[1] Department of Physics and Astronomy, University of Nebraska–Lincoln, Lincoln, NE 68588-0299, United States of America
[2] CEA, DAM, DIF, F-91297 Arpajon, France
[3] The Pennsylvania State University, Hazleton, PA 18202, United States of America
[4] Correspondence to: Leidos Inc., 2109 Air Park Rd. SE, Ste. 200, Albuquerque, NM 87106, United States of America.

E-mail: s.kalmykov.2013@ieee.org

Keywords: laser wakefield accelerator, blowout, optical control of injection, comb-like electron beams, pulse stacking, negative chirp, inverse Compton/Thomson scattering

Abstract

Generating quasi-monochromatic, femtosecond γ-ray pulses via Thomson scattering (TS) demands exceptional electron beam (e-beam) quality, such as percent-scale energy spread and five-dimensional brightness over 10^{16} A m^{-2}. We show that near-GeV e-beams with these metrics can be accelerated in a cavity of electron density, driven with an incoherent stack of Joule-scale laser pulses through a mm-size, dense plasma ($n_0 \sim 10^{19}$ cm^{-3}). Changing the time delay, frequency difference, and energy ratio of the stack components controls the e-beam phase space on the femtosecond scale, while the modest energy of the optical driver helps afford kHz-scale repetition rate at manageable average power. Blue-shifting one stack component by a considerable fraction of the carrier frequency makes the stack immune to self-compression. This, in turn, minimizes uncontrolled variation in the cavity shape, suppressing continuous injection of ambient plasma electrons, preserving a single, ultra-bright electron bunch. In addition, weak focusing of the trailing component of the stack induces periodic injection, generating, in a single shot, a train of bunches with controllable energy spacing and femtosecond synchronization. These designer e-beams, inaccessible to conventional acceleration methods, generate, via TS, gigawatt γ-ray pulses (or multi-color pulse trains) with the mean energy in the range of interest for nuclear photonics (4–16 MeV), containing over 10^6 photons within a microsteradian-scale observation cone.

1. Introduction

Inverse Compton scattering [1–8] is an emerging technique for obtaining quasi-monochromatic, strongly collimated γ-ray pulses through the collision of a short, quasi-monoenergetic electron beam (QME e-beam) and a near- to mid-IR interaction laser pulse (ILP). During the interaction, relativistic electrons, propagating at an angle to the ILP, experience its Lorentz-compressed wave front, the maximum compression occurring along the e-beam direction. As they oscillate in the ILP electromagnetic field, electrons emit radiation, scattering the compressed wave front. An observer in the far field thus detects an angular distribution of high-energy photons, with their energy being the highest for a detector placed in the e-beam direction. For the head-on collision, the ILP photon energy is Doppler upshifted by a factor of $4\gamma_e^2$, where γ_e is the electron Lorentz factor. A 900 MeV electron thus converts a 1.5 eV ILP photon into a 19 MeV γ-photon. As the energy of emitted photons is much lower than the electron energy, the recoil is negligible. This low-energy semi-classical limit of the general quantum-mechanical inverse Compton scattering, known as Thomson scattering (TS), is the subject of this paper. As the e-beam phase space imprints itself onto the energy spectrum and γ-ray emission pattern, characteristics of the γ-ray source are sensitive to modulations in e-beam current and/or a chirp in its longitudinal momentum [9–12].

The production of multi-picosecond TS γ-ray pulses has been earlier demonstrated using e-beams from conventional accelerators [12–21]. These pulses have a high degree of polarization, and are thus attractive as e-beam diagnostics [12, 13]. They are also employed in the generation of polarized positrons from dense targets [15] and to demonstrate nuclear fluorescence [17–19, 21]. Conventional accelerators, however, are large and expensive, which makes linac-based radiation sources scarce and busy user facilities. Also, the large (cm-scale) size of the radio-frequency powered acceleration cavities makes it difficult to produce and synchronize e-beams (and, hence, TS γ-ray pulses) on a sub-ps time scale relevant to high-energy density physics [22]. Luckily, an alternative technical solution, a miniature laser–plasma accelerator (LPA) [23, 24], enables production of even shorter (viz. femtosecond) e-beams [25]. Besides, polychromatic (or 'comb-like') beams from an LPA, with the current modulated on a femtosecond scale, have been observed in experiments [26–29]. Simulations indicate that such beams readily lend themselves to all-optical manipulation, promising generation of spectrally controlled quasi-monochromatic, femtosecond γ-ray pulses, or trains of pulses with a femtosecond synchronization [9–11].

LPAs, however, face a number of challenges, one of which is preservation of beam quality, that is, elimination of a high-charge, low-energy tail, which develops when acceleration is continued through electron dephasing [30–34]. In experiments, TS from these imperfect LPA e-beams [35–40], along with a tendency to scale photon energy up to ~10 MeV [41–45], results in large γ-ray bandwidth, which is incompatible with applications in nuclear forensics and radiography [6, 8, 19, 21]. The second challenge comes from the widely cited scaling [46] that prescribes using PW-scale laser pulses and cm-length plasmas in order to compete with GeV linacs. This frustrates radiation physics applications dependent on dosage, as the required kHz repetition rates translate, in this case, into megawatt average laser power that pertains to the technology of distant future [47, 48]. Both challenges are rooted in the degradation of the LPA driver—a relativistically intense, multi-terawatt, sub-100 fs laser pulse—as it imparts the energy into the plasma. To realize full potential of the LPA in radiation physics [49], it is thus necessary to understand and control relativistic optical phenomena underlying this degradation [34, 50].

In a conventional LPA, the ponderomotive force of the laser pulse creates a cavity in the electron fluid, while the ions, due to their high inertia, remain approximately at rest. The pulse drives this 'bubble' over many Rayleigh lengths [51, 52]. The co-moving perturbation of the nonlinear index of refraction red-shifts the pulse leading edge by a considerable fraction of the carrier frequency ω_0, while anomalous group velocity dispersion of the plasma compresses the pulse into a sub-cycle relativistic optical shock [34, 50]. Diffraction of the pulse leading edge contributes to the pulse self-steepening[5]. Self-compression of the pulse is responsible for electron dephasing, and is thus the major factor limiting the energy gain. It also causes uncontrolled deformation of the cavity, facilitating massive continuous self-injection of ambient electrons (dark current). It was shown earlier that, by incoherently mixing the pulse at the fundamental frequency with a frequency-upshifted pulse of the same, or lower, energy (on a sub-Joule scale), it is possible to design an optical driver resilient to self-compression (at least on the time scale of electron dephasing) [55]. By thus minimizing variations in the size of accelerating cavity, one suppresses continuous electron injection, preserving a single QME bunch with an ultrahigh five-dimensional (5D) brightness exceeding 10^{16} A m^{-2}. Brightness in this range is clearly an advantage for the design of TS light sources [56, 57]. Our simulations show that emulating a step-wise negative chirp, by advancing the higher-frequency component of the stack in time, nearly doubles electron energy compared to the predictions of the accepted scalings, demonstrating a near-GeV gain in a mm-scale, dense plasma ($n_0 \sim 10^{19}$ cm^{-3}) along with a boost in brightness to a few 10^{17} A m^{-2}. These ultra-bright bunches are perfectly suited to generate, via TS, femtosecond-length, gigawatt γ-ray pulses with a 15%–20% bandwidth and the mean energy in the range of interest for nuclear photonics, 4–16 MeV [8]. In addition, weak focusing of the lower-frequency, trailing component of the stack enforces periodic injection, controllably producing synchronized sequences of femtosecond electron bunches (e-bunches). These bunch trains emit, via TS, polychromatic γ-ray beams containing up to three distinct bands with controlled energy spacing, and over 10^6 photons per shot in a microsteradian-scale observation cone. The modest footprint and Joule-scale laser energy of the stack-driven LPA promises an increase in the repetition rate to hundreds of Hz, at kW average power, enabling radiation physics applications dependent on dosage. From the viewpoint of laboratory practice, kHz-scale repetition rate and low pulse energy enable computerized manipulations of the phase and shape of the sub-Joule stack components, using adaptive optics and genetic algorithms [58, 59], aiding in real-time optimization of e-beam parameters.

The paper is organized as follows. Section 2 describes the computational approach and defines parameters of the case studies. These parameters are representative of LPA experiments carried out in numerous laboratories worldwide. The reported case studies may thus serve as a reference for practical realization of the scheme in an

[5] Diffraction of the leading edge may be suppressed by propagating the pulse in a preformed channel [9] or in a bucket of a plasma wake driven by a co-propagating pre-pulse [53, 54].

existing experimental setting. Section 3 concentrates on the generation of comb-like e-beams and of synchronized, polychromatic trains of γ-ray pulses. Control over the electron phase space through independent focusing of the stack components is demonstrated. Section 4 explores all-optical control over parameters of QME e-bunches, through variation of the difference frequency and time delay between the stack components. It is shown that almost 80% increase in electron energy and a factor 4.5 increase in brightness may be achieved with the same target and laser energy. This permits tuning the energy of TS γ-ray pulses in the range 4–16 MeV, without losing photons, keeping the low-energy background at a modest level. Appendix A addresses spectral features of TS from weakly collimated e-beams, to help estimate collimation of the photon pulse and to support observations made in section 3.2. Appendices B and C show that a more than a 50% reduction in the energy of the blue-shifted stack component reduces the e-beam energy by merely 25%, while not degrading the e-beam in other aspects. Section 5 summarizes the results and points out directions of future work.

2. Interaction regimes and simulation methods

Manipulations of e-beam phase space are explored using the relativistic, fully explicit, quasi-cylindrical particle-in-cell code CALDER-Circ [60]. CALDER-Circ preserves realistic interaction geometry and accounts for the axial asymmetry and polarization of the fields by decomposing all electromagnetic fields and currents into a set of azimuthal modes (whereas the macroparticles are pushed in the three-dimensional Cartesian space). If the laser pulse envelope is initially cylindrically symmetric, using the two lowest order modes does not compromise the accuracy of simulation [61]. This reduces the three-dimensional problem to an essentially two-dimensional one, permitting economical usage of high-performance computational resources. In addition, CALDER-Circ uses a numerical Cherenkov-free electromagnetic solver [62] and third-order splines for the macroparticles. These features, in combination with a fine grid ($\Delta z = 0.125c/\omega_{\rm tail} \approx 16$ nm, $\Delta r \approx 16\Delta z$, where $r^2 = x^2 + y^2$, and $\omega_{\rm tail}$ is defined below), small time step ($\omega_{\rm tail}\Delta t = 0.1244$), and 45 macroparticles per cell, maintain low sampling noise, negligible numerical dispersion, and avoid numerical emittance dilution. The physical setup is the same as in [55]. The plasma begins at $z = 0$ with a 0.5 mm linear ramp, followed by a uniform section with the density $n_0 = 6.5 \times 10^{18}$ cm^{-3}. A bi-color stack of transform-limited, linearly polarized Gaussian pulses, propagating towards positive z, is focused at the plasma border. The electric field in the focal plane is

$$\mathbf{E}_\perp(x, y, z = 0, t) = \mathbf{E}_{\rm tail} + \mathbf{E}_{\rm head}, \tag{1}$$

where

$$|e|\mathbf{E}_{\rm head}/(m_e\omega_{\rm tail}c) = \mathbf{e}_y\mathcal{E}_{\rm head}\mathrm{e}^{-\mathrm{i}\omega_{\rm head}t - 2\ln 2\, t^2/\tau_L^2 - r^2/r_{\rm head}^2}, \tag{2}$$

$$|e|\mathbf{E}_{\rm tail}/(m_e\omega_{\rm tail}c) = \mathbf{e}_x\mathcal{E}_{\rm tail}\mathrm{e}^{-\mathrm{i}\omega_{\rm tail}(t-T) - 2\ln 2(t-T)^2/\tau_L^2 - r^2/r_{\rm tail}^2}. \tag{3}$$

Here, $-|e|$ and m_e are the electron charge and rest mass, c is the speed of light in vacuum, $\omega_{\rm head} > \omega_{\rm tail}$, and $\mathbf{e}_{x,y}$ are unit polarization vectors. Throughout the paper, the spot size of the leading pulse is fixed at $r_{\rm head} = 13.6$ μm. The frequency of the trailing pulse is fixed as well, so that its wavelength is always $\lambda_{\rm tail} = 2\pi c/\omega_{\rm tail} = 0.805$ μm. This yields the normalization constant $m_e\omega_{\rm tail}c/|e| = 4$ TV m^{-1}.

The reference regime corresponds to a single transform-limited 70 TW pulse [10, 34]: $\mathcal{E}_{\rm head} = 0$, $\mathcal{E}_{\rm tail} = 3.27$, $\tau_L = 30$ fs. The reference pulse depletes soon after electron dephasing, a strategy often suggested to maximize acceleration efficiency and monochromatize e-beam via phase space rotation at the end of the acceleration cycle [46]. Contrary to common expectations, this approach leads to copious dark current and overall low beam quality [10, 34], a direct consequence of the dynamics associated with red-shifting (and hence catastrophic self-compression) of the pulse as it approaches depletion [34, 50, 63]. This can be avoided by tailoring the laser pulse phase. To achieve meaningful control, however, the pulse bandwidth must be comparable with the carrier frequency. Then, the nonlinear red-shift imparted by the plasma wakefield to the pulse leading edge may be compensated by the negative frequency chirp. The pulse thus remains uncompressed, and acceleration almost dark-current-free through electron dephasing [9, 10, 50]. One practical way to synthesize a negative step-wise chirp is by optically mixing independent, transform-limited, narrow-bandwidth blocks of the same or different energy, advancing the blue-shifted component in time by $T \sim \tau_L$ [55]. This incoherent stacking is expressed in equations (1)–(3). The frequency ratio ($\Omega = \omega_{\rm head}/\omega_{\rm tail} > 1$), the ratio of the spot sizes ($R = r_{\rm head}/r_{\rm tail}$), time delay ($T > 0$), and the energy partition are all-optical control knobs that permit tuning e-beam parameters.

In section 3, we concentrate on the stack with an optimal delay T that permits about 80% electron energy boost compared to the prediction of the standard scaling [55]. By focusing the stack components differently (i.e. having $R \neq 1$), it appears possible to either keep the beam QME (for $R \geq 1$), or to generate a train of bright QME bunches of different energies (for $R < 1$) [11]. In the latter case, TS produces a train of spectrally distinct, narrow bandwidth γ-ray pulses. In section 4, we carry out multi-parametric scans (varying all parameters except $R = 1$),

demonstrating optical control over the production of a single high-brightness e-bunch, to drive a narrow-bandwidth γ-ray pulse via TS.

To simulate TS [7], we extract N_b macroparticles from the first and second buckets of the wake, sampling the six-dimensional (6D) phase space of the e-beam. Using these initial conditions, electrons are propagated in free space by solving the relativistic equations of motion. In the absence of a laser field, their trajectories are ballistic. The e-beam collides head-on with the ILP, which is linearly polarized in the x-direction and specified analytically in the paraxial approximation. The ILP has a 0.8 μm carrier wavelength (photon energy $E_{\rm int} = 1.5$ eV), 250 fs duration corresponding to 0.3% FWHM bandwidth in spectral intensity, and 16.8 μm waist size (Rayleigh length 1.1 mm). The timing between the e-beam and the ILP is chosen so that the centroid of the beam and the peak of the ILP intensity arrive at the ILP focal plane simultaneously. Since in all regimes under consideration the e-beams appear to be relativistic and low-density, $n_e\langle\gamma_e\rangle^{-3} \ll 10^{16}\,{\rm cm}^{-3}$, space charge forces are neglected [2, 3]. Radiation damping is also neglected, as the energy emitted by an electron passing through the ILP is small compared to the energy of the electron. As the ILP is shorter than 7% of its Rayleigh length and the e-beam spot size is in the sub-micron range, the interaction occurs in nearly plane-wave geometry. To avoid broadening the TS spectra [4, 5, 43], a linear interaction regime is chosen, with the ILP normalized vector potential $a_{\rm int} = 0.1$ (hence the ILP energy 25.5 mJ). Once the orbits of individual electrons are obtained, taking a weighted average over the ensemble yields the mean energy density radiated per unit frequency ω and solid angle Ω per electron [64]:

$$\frac{{\rm d}^2 I_e}{{\rm d}\omega{\rm d}\Omega} = \frac{e^2\omega^2}{4\pi^2 c}\left(\sum_{i=1}^{N_b} w_i\right)^{-1}\sum_{i=1}^{N_b} w_i\left|\int_{-\infty}^{\infty}\mathbf{n}\times(\mathbf{n}\times\boldsymbol{\beta}_i)\,{\rm e}^{{\rm i}\omega(t-\mathbf{n}\cdot\mathbf{r}_i(t)/c)}{\rm d}t\right|^2.$$

Here, w_i is the macroparticle weight, $\mathbf{n}$ is the unit observation vector, and $\mathbf{r}_i$ and $\boldsymbol{\beta}_i = \mathbf{v}_i/c$ are the radius vector and normalized velocity of the electron, respectively. The total energy radiated by the beam with a charge Q is ${\rm d}^2 I_{\rm tot}/{\rm d}\omega{\rm d}\Omega = (Q/|e|)\,{\rm d}^2 I_e/{\rm d}\omega{\rm d}\Omega$. In all cases except figure 3, we show the TS spectra for the emission in the polarization plane of ILP, in the direction of e-beam propagation (i.e. on-axis observation).

3. Generating trains of e-bunches and comb-like γ-ray beams

3.1. Parameters of case studies

We start with a stack of equal-energy (0.7 J), same-duration ($\tau_L = 20$ fs) pulses with matched spots, $R = 1$; hence $\mathcal{E}_{\rm head} = \mathcal{E}_{\rm tail} = 2.31$. A frequency ratio $\Omega = 1.5$ and delay $T = 3\tau_L/4 = 15$ fs, corresponding to the case S-A2 of [55], are optimal for QME e-beam production. Propagating the stack in a preformed plasma channel induces periodic focusing in its tail [9]. Resulting variations in the bubble size cause periodic self-injection and production of a sequence of QME e-bunches in a single shot [55]. Here, we achieve the same effect in the uniform plasma, by focusing the stack components differently. To examine the trend, we define the following five cases:

- Stack A1: $R = 2^{1/2}$, $\mathcal{E}_{\rm tail} = 3.27$;
- Stack A2: $R = 1$ (S-A2 equivalent [55]);
- Stack A3: $R = (3/2)^{-1/2}$, $\mathcal{E}_{\rm tail} = 2.83$;
- Stack A4: $R = 2^{-1/2}$, $\mathcal{E}_{\rm tail} = 1.63$;
- Stack A5: $R = 3^{-1/2}$, $\mathcal{E}_{\rm tail} = 1.33$.

Section 3.2 shows that strong focusing in the tail (case A1) preserves QME acceleration. Weak focusing, on the other hand, induces periodic focusing in the tail, producing trains of two (A2) or three e-bunches (A4, A5). Section 3.3 highlights the dynamics of bunch train production in the case A4. The entire trend is exposed in section 3.4, where we show that trains of e-bunches are perfectly suited to generate, in a controllable fashion, multi-color trains of TS γ-ray pulses. Statistics of QME e-beams at dephasing and corresponding partial TS γ-ray signals are presented in tables 1 and 2.

3.2. Stack with over-focused tail (A1) steadily self-guides, driving single e-bunch

In case A1, expansion and stabilization of the bubble between $z = 0.76$ and 1.52 mm, as seen in figures 1(a) and (c), creates the QME e-bunch. By dephasing ($z_{\rm deph} = 3.11$ mm), this bunch receives a 75% boost in energy compared to the reference case (see figure 2(a)), while absorbing 5.2% of the laser energy. According to test particle simulations carried out with WAKE [65], beam loading [66] reduces electron energy by 25% in the reference case, and merely by a few percent in case A1. The observed energy boost is thus explained almost

Table 1. Statistics of QME e-bunches at dephasing in cases A1–A5 (only electrons from the first bucket are included). In the reference case, electrons are selected from the energy interval between 400 and 625 MeV, so that the high-energy tail is not included. Q is the charge; $\langle E\rangle$ is the mean energy; σ_E is the energy variance; σ_τ is the RMS length; σ_α is the RMS divergence; $\varepsilon_\perp^N$ is the RMS normalized transverse emittance; B_n is the 5D brightness; W is the total energy of the bunch.

Parameter Units	Q pC	$\langle E\rangle$ MeV	σ_E MeV	σ_τ fs	σ_α mrad	$\varepsilon_\perp^N$ mm mrad	B_n 10^{17} A m^{-2}	W mJ
Reference	275.0	505.0	45.0	3.40	1.95	0.50	0.66	138.9
A1	83.4	873.2	35.2	1.08	1.61	0.48	0.68	72.8
A2	73.1	882.0	28.7	0.85	1.35	0.40	1.09	64.5
A3 (I)	69.7	868.7	21.8	0.78	1.35	0.40	1.12	60.5
A3 (II)	43.5	591.5	26.5	1.06	1.91	0.41	0.50	25.7
A4 (I)	57.7	873.0	21.3	0.74	1.45	0.41	0.96	50.4
A4 (II)	29.5	583.3	18.5	0.96	1.70	0.38	0.44	17.2
A4 (III)	64.2	383.2	54.5	2.41	3.44	0.72	0.11	24.6
A5 (I)	27.4	914.0	40.3	0.61	1.10	0.40	0.59	25.0
A5 (II)	18.8	574.7	17.6	0.78	1.80	0.38	0.33	10.8
A5 (III)	24.5	362.0	25.9	1.66	3.40	0.63	0.08	8.9

Table 2. Statistics of γ-rays emitted by the bunches with parameters from table 1. Corresponding energy spectra are depicted in black (I), gray (II), and light gray (III) in figures 7(a.2)–(e.2). $\langle E_{\rm ph}\rangle$ is the mean energy; σ_E is the energy variance; $N_{\rm ph}$ and $W_{\rm ph} = N_{\rm ph}\langle E_{\rm ph}\rangle$ are the number of photons and energy radiated into the observation solid angle $\Delta\Omega_{\rm ph} = (\pi/2)\langle\gamma_e\rangle^{-2}$ in the direction of e-beam propagation.

Parameter	$\langle E_{\rm ph}\rangle$ (MeV)	σ_E (MeV)	$\Delta\Omega_{\rm ph}$ (μsr)	$N_{\rm ph}$ ($\times 10^6$)	$W_{\rm ph}$ (μJ)
Reference	5.61	1.06	1.61	4.81	4.32
A1	15.4	2.91	0.54	1.71	4.21
A2	16.0	2.51	0.53	1.56	4.00
A3 (I)	15.8	2.33	0.54	1.63	4.11
A3 (II)	7.15	1.31	1.17	0.73	0.83
A4 (I)	15.8	2.48	0.54	1.25	3.14
A4 (II)	7.26	1.07	1.21	0.62	0.72
A4 (III)	2.78	0.54	2.80	0.91	0.41
A5 (I)	17.3	2.55	0.49	0.49	1.36
A5 (II)	7.06	1.08	1.24	0.38	0.43
A5 (III)	2.80	0.55	3.13	0.38	0.17

entirely by the changes in quasistatic bubble dynamics brought forth by changes in the dynamics of optical driver. From $z = 1.67$ mm (gray in figure 2(a)) through dephasing (black in figure 2(a)), the slowly expanding bubble injects 250 pC; this is only 15% of the tail charge in the reference case. Collection phase space (longitudinal momenta of electrons crossing the plane $z = z_{\rm deph}$ shown against their initial positions in figure 1(c)) and collection volume (initial radial positions versus initial longitudinal positions, figure 1(d)) corroborate this interpretation. At dephasing, the average flux in the tail is below 30% of the peak value of dN/dE in the QME component. At the same time, the divergence of low-energy electrons is a factor 3 higher, on average. This keeps emission of low-energy photons in the beam propagation direction at a fairly low level (gray in figure 3(b)). As a result, figure 2(b) shows minimal degradation of the γ-ray signal as its mean energy increases from 5 MeV to 15 MeV.

The entry A1 in table 1 shows e-bunch statistics at dephasing (black in figure 3(a)). The extremely high 5D brightness of this 80 kA bunch, $B_n = 2\langle I\rangle(\pi\varepsilon_\perp^N)^{-2} \approx 7\times 10^{16}$ A m^{-2} [56], is most promising for a TS light source [57]. Here, $\langle I\rangle = Q/\sigma_\tau$ is the mean current; Q is the charge; σ_τ is the root-mean-square bunch length; and $\varepsilon_\perp^N = 2^{-1/2}[(\varepsilon_x^N)^2 + (\varepsilon_y^N)^2]^{1/2}$, with $\varepsilon_i^N = (m_e c)^{-1}[(\langle p_i^2\rangle - \langle p_i\rangle^2)(\langle r_i^2\rangle - \langle r_i\rangle^2) - (\langle p_i r_i\rangle - \langle r_i\rangle\langle p_i\rangle)^2]^{1/2}$, is the RMS normalized transverse emittance. In the absence of numerical Cherenkov radiation, $\varepsilon_\perp^N$ increases by 10% as electrons reach dephasing. Thus any degradation of the TS γ-ray signal observed in the simulations must be attributed to the physical causes rather than to numerical artifacts. The RMS divergence of the bunch A1, even at dephasing, remains quite high, $\sigma_\alpha \approx 1.6$ mrad $\approx 2.75\langle\gamma_e\rangle^{-1}$, where $\sigma_\alpha = 2^{-1/2}(\sigma_x^2(\alpha) + \sigma_y^2(\alpha))^{1/2}$, and $\sigma_i(\alpha) = \langle p_z\rangle^{-1}(\langle p_i^2\rangle - \langle p_i\rangle^2)^{1/2}$. Weak collimation of electrons, combined with their 4% energy spread, directly affects both collimation and energy spread of TS γ-rays.

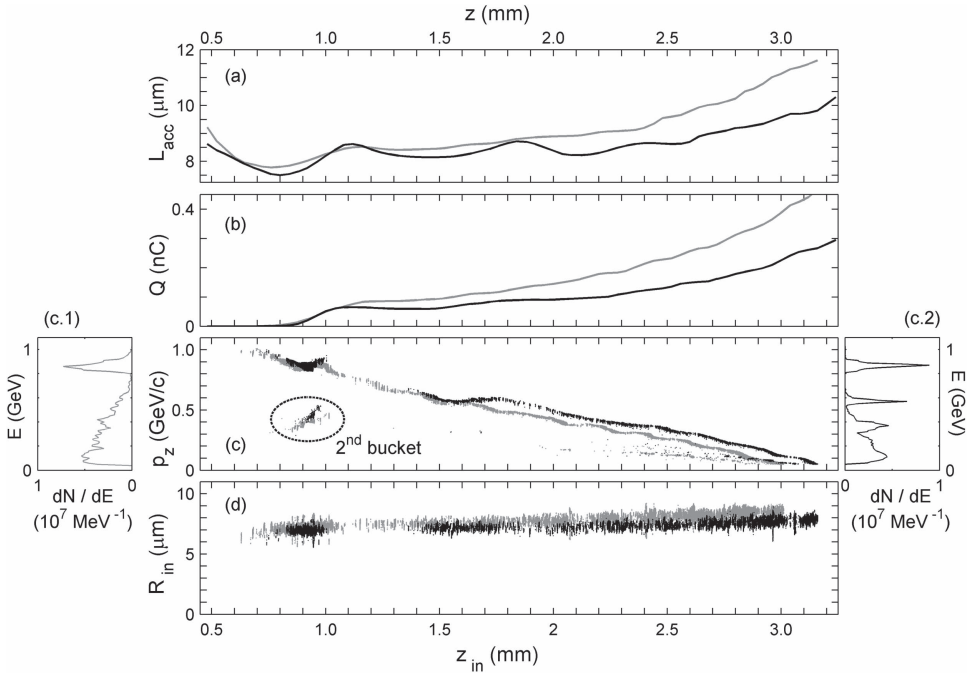

Figure 1. Kinetics of self-injection leading to generation of QME (case A1, gray) and comb-like e-beams (case A4, black). (a) The length of accelerating phase on axis (roughly, half-length of the bubble) and (b) the charge of electrons with energy above 50 MeV versus propagation distance. The charge accumulates in the bubble only during intervals of its expansion. This is corroborated by the display of (c) collection phase space (final longitudinal momenta of electrons versus their initial positions; the ellipse encircles particles accelerated in the second bucket) and (d) collection volume (initial radial positions versus initial longitudinal positions). Corresponding energy spectra are shown in the sub-panels (c.1), (c.2). Periodic focusing in the tail of stack A4 forces oscillation in the bubble size (seen in (a)). Hence the periodic injection and formation of the electron energy comb (panel (c.2)).

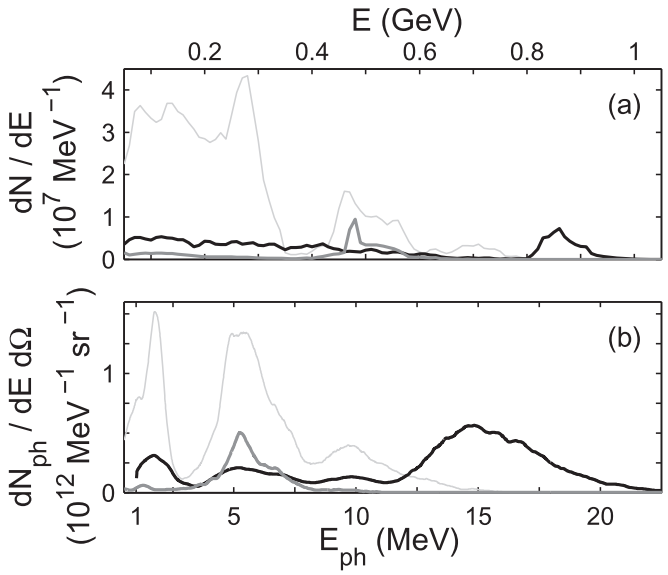

Figure 2. The stack A1 (over-focused tail) generates a QME e-bunch; the bunch drives a low-background TS γ-ray signal. (a) Electron energy spectra are shown prior to dephasing ($z = 1.67$ mm, gray) and at dephasing ($z_{deph} = 3.11$ mm, black). Thin light gray curve shows the spectrum at dephasing in the reference case ($z_{deph} = 2.11$ mm). Corresponding TS γ-ray spectra are shown in panel (b). Stacking suppresses low-energy background in both electron and γ-ray signal. Electrons receive 75% energy boost against the reference case, while the mean energy of γ-rays triples.

The collimation of high-energy γ-photons, as well as the number of photons in the observation cone, are important metrics for applications. To evaluate the reduction in photon energy and flux with an increase in the observation angle (viz. to estimate the effective apex angle of the photon emission cone), we select the macroparticles making up the QME e-bunch, as shown in figure 3(a), and carry out the TS simulation with these initial conditions. The results are displayed in figures 3(b)–(d); black curves show the photon flux per unit solid

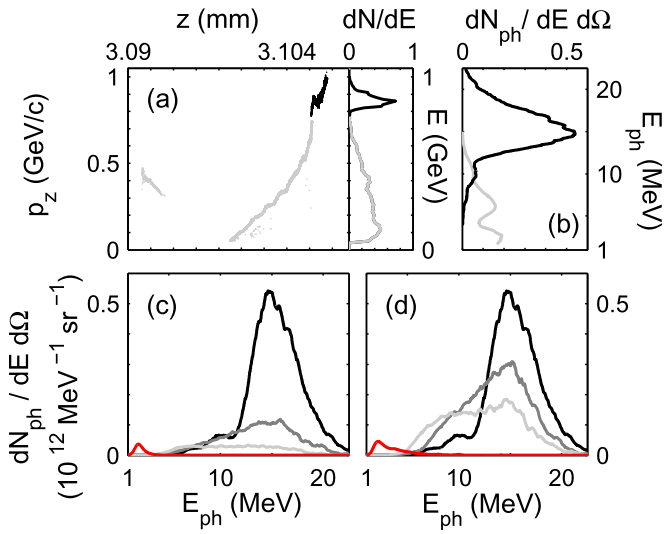

Figure 3. Case A1: QME e-bunch extracted at dephasing emits well collimated TS γ-photons. (a) Longitudinal phase space of the bunch; inset: energy spectrum in units 10^7 MeV^{-1}. (b) Spectrum of γ-rays emitted in the direction of e-beam propagation (same units as in (c) and (d)). QME components of electron and γ-ray beams are depicted in black. (c), (d) Spectrum of γ-rays emitted by the QME e-bunch (c) in the polarization plane of the ILP ($\phi = 0$) and (d) in the orthogonal plane ($\phi = \pi/2$). The signal is detected in the direction of e-beam propagation ($\theta = 0$, black, same as in (b)), and at angles $\theta_1 = 2^{-1/2}\langle\gamma_e\rangle^{-1} \approx 0.415$ mrad (gray), $\theta_2 = \langle\gamma_e\rangle^{-1}$ (light gray), $\theta_3 = \sigma_\alpha \approx 1.61$ mrad (red). There are virtually no high-energy photons ($E_{\rm ph} > 10$ MeV) outside the observation cone with the apex angle $2\theta_2$.

angle, in the direction of e-beam propagation (on-axis observation, $\theta = 0$, where the detection angle is measured from the direction of e-beam propagation). The QME photon signal is centered at $\langle E_{\rm ph}\rangle \approx 15.4$ MeV, and has a 19% RMS energy spread. The other curves in figures 3(c) and (d) correspond to scattering under a gradually increasing angle: $\theta = 2^{-1/2}\langle\gamma_e\rangle^{-1}$, $\langle\gamma_e\rangle^{-1}$, and σ_α. From spectra in figures 3(c) and (d), the mean photon energy drops only by 25% as θ increases from zero to $\langle\gamma_e\rangle^{-1}$, which agrees with semi-analytic estimates of appendix A. Conversely, the photon flux drops rather sharply. To a good approximation, there are virtually no photons with the energies above 10 MeV outside the observation cone of apex angle $2\theta = 2\langle\gamma_e\rangle^{-1}$. Thus, to estimate the number of QME high-energy photons scattered in the direction of e-beam propagation, we conservatively choose the observation solid angle $\Delta\Omega_{\rm ph} = (\pi/2)\langle\gamma_e\rangle^{-2}$, i.e. the solid angle of the cone with an apex angle $2\theta_1 = \sqrt{2}\,\langle\gamma_e\rangle^{-1}$ ($\approx 2 \times 0.415$ mrad in case A1), take the photon flux corresponding to the direct backscattering ($\theta = 0$), integrate it over the energy, and multiply the result by $\Delta\Omega_{\rm ph}$. As the QME e-bunch accelerates through dephasing, we extract its phase space at different locations in the plasma, and use this in the TS simulations, tracking statistics of the QME γ-ray signal (the statistics at the dephasing point makes the entry A1 in table 2). This yields an interesting observation: the average energy of the QME photon signal A1 may be varied from 5 to 15 MeV without losing photons in the observation cone, keeping $N_{\rm ph} \approx 1.7(\pm 0.05) \times 10^6$. This is a direct consequence of the e-bunch emittance preservation.

Figures 3(c) and (d) suggest noticeable asymmetry of the photon beam, with a larger divergence in the y-direction (orthogonal to the ILP polarization). This may be explained by the fact that the e-beam is not quite symmetric, with about 30% smaller divergence in the x-direction ($\sigma_x(\alpha) = 1.4$ mrad and $\sigma_y(\alpha) = 1.8$ mrad), resulting in flattening of the TS γ-ray pulse.

Figure 4 reveals the source of considerable energy spread in a typical TS γ-ray pulse. We take the QME e-bunch at dephasing (the region of phase space depicted with black markers in figure 3(a)), and plot the energy spectrum of TS photons emitted by the bunch using the complete 6D phase space (the same as in figure 3(b)). It appears that the 19% spread in γ-ray energy (see entry A1 in table 2) is imparted almost entirely by the 4% energy spread in the e-bunch. This is proven in a pair of test TS simulations with artificially reduced electron phase space. First, $p_z = \langle p_z\rangle = 1705 m_e c$ is assigned to all electrons, while p_x and p_y are unchanged. This preserves mrad-scale divergence of the bunch, with near-zero energy spread. In the second case, the transverse momenta are set to zero, while p_z is unchanged, preserving the energy spread with zero divergence. The first case yields a monoenergetic TS signal (sub-percent energy spread), plotted in black in figure 4(a), centered at $E_{\rm ph} \approx 4\langle\gamma_e\rangle^2 E_{\rm int}$. Conversely, the photon signal from the second case (black in figure 4(b)) retains a 13% energy spread.

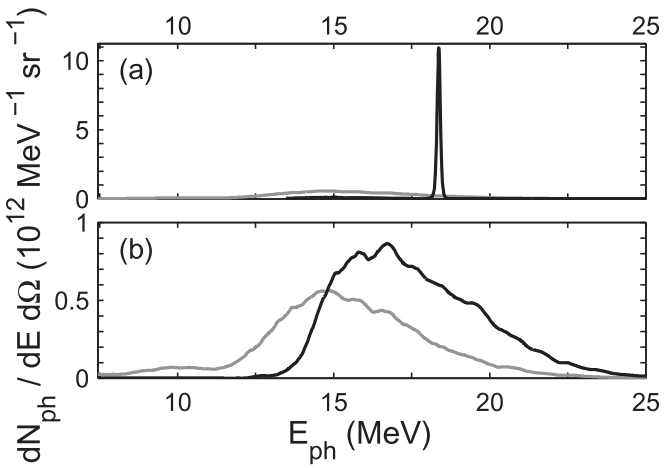

Figure 4. Case A1: energy spread of TS γ-photons emitted by the QME e-bunch (same bunch as in figure 3) is determined by the energy spread in the bunch. Gray: the spectrum of TS photons emitted by electrons with the complete phase space (same as black in figures 3(b)–(d)). Black: simulations with the reduced phase space of electrons, with (a) zero dispersion of longitudinal momentum (viz. almost vanishing energy spread) and (b) zero dispersion of transverse momentum (zero divergence).

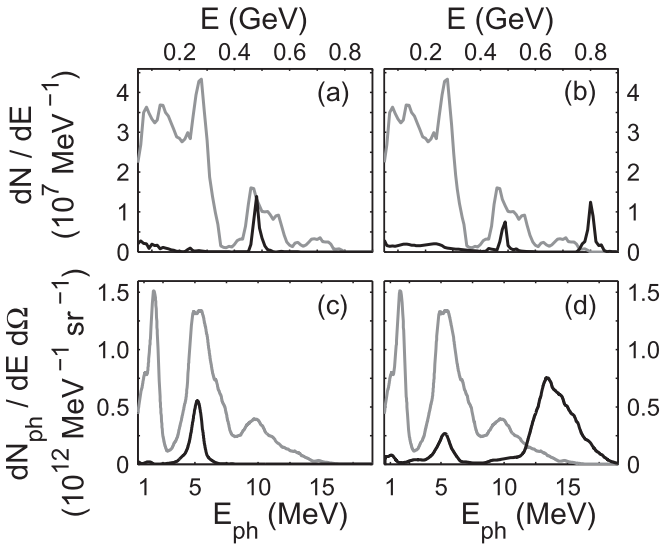

Figure 5. Generating bi-color electron and γ-ray beams using a stacked driver with a weakly focused tail (A4). Energy spectra of e-beams are shown at (a) $z = 1.59$ mm and (b) $z = 2.63$ mm; spectra of corresponding TS γ-ray signals are shown in panels (c) and (d). Gray: the electron and photon spectra in the reference case at dephasing (same as in figure 2).

3.3. Stack with weakly focused tail (A4): creating a train of e-bunches

The stack with an over-focused tail maintains a single, high-brightness QME e-bunch through dephasing. Yet the residual low-energy tail—the region of phase space plotted with gray markers in figure 3(a)—contains approximately 300 pC, which is 3.5 times the charge of the QME bunch. To make this considerable charge useful, we may enforce phase space bunching of the low-energy electrons, transforming the continuous background into a set of compact QME bunches of high brightness, with femtosecond-scale synchronization, as seen in figure 6(a). It appears that weak focusing of the stack tail results in periodic self-focusing of the tail. Ensuing oscillation in the bubble size, seen in figure 1(a), generates a pair of QME bunches, labeled I and II in figure 6(a). Evolution of their energy spectra through dephasing is shown in figures 5(a) and (b). Figure 1(c) indicates that charge accumulates without interruption after $z = 2.2$ mm. Yet, the brief stabilization of the bubble around $z = 2.5$ mm monochromatizes the group of earlier injected particles, adding a third QME component to the energy comb, beam III in figure 6(a). By dephasing, the tri-color e-beam absorbs 6.5% of the laser energy. Entries A4(I)–A4(III) in table 1 show statistics of e-bunches at dephasing ($z_{\rm deph} \approx 3.2$ mm, see figure 6(a)). The bunches accelerated in the first wake bucket have a fairly high current, (I) 77 kA, (II) 31 kA, (III) 27 kA, which translates into their 10^{16}–10^{17} A m^{-2} brightness. The bunch from the second bucket has a modest current (3.8 kA) and low brightness (3×10^{15} A m^{-2}). Its contribution to the TS signal is thus negligible.

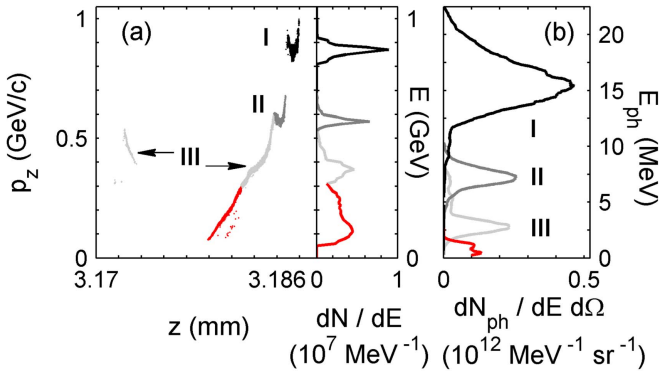

Figure 6. Photon energy comb emitted by a train of e-bunches. (a) Longitudinal phase space and energy spectrum (inset) of the bunch train accelerated through dephasing with the stack A4 ($z \approx 3.2$ mm). (b) The TS γ-ray signal, split into partial signals from the QME bunches (I)–(III). Red: residual energy tail in electron and photon beams.

To calculate the spectrum of γ-rays radiated by a selected QME e-bunch into the observation solid angle $\Delta\Omega_{\rm ph} = (\pi/2)\langle\gamma_e\rangle^{-2}$, in the bunch propagation direction, we split the electron phase space into groups of macroparticles corresponding to the distinct QME features, as shown in figure 6(a), and apply the procedure described in section 2 to each group. The sum of these partial spectra yields the total photon spectra, such as displayed in figures 5(c) and (d). These spectra consist of a single- and a bi-color signals with virtually no background. Energy spectra of partial γ-ray signals, from a tri-color e-beam near dephasing, shown in figure 6(b), reveal virtually no overlap. Their statistics makes entries A4(I)–A4(III) in table 2. A weak low-energy energy tail in the e-beam ($E < 300$ MeV, red in figure 6(a)) makes a barely noticeable addition to the TS spectrum (red in figure 6(b)). From table 2, the photon energy bands have a 15%–20% RMS energy spread. As the divergence of e-bunches is large, $\langle\gamma_e\rangle\sigma_\alpha > 1$, integrating the partial photon spectrum over energy and multiplying the result by $\Delta\Omega_{\rm ph}$ corresponding to the band yields the total number of photons in the band, in the μsr-scale observation angle. From table 2, this number is of the order of 10^6, which is comparable to the experimental findings with 100 MeV scale e-beams, $3 \times (10^5$–$10^7)$ [39, 41, 42]. Yet, our highest-energy photons reach 15 MeV while preserving a 15% energy spread and microsteradian divergence, which is strikingly better than 50%–100% spread and milli-steradian divergence reported for the sub-MeV photons [39, 41, 42].

3.4. Trains of e-bunches emit spectrally resolved combs of γ-ray beams

Weak focusing of the stack tail sets in periodic focusing that alters the kinetics of self-injection, creating additional QME bunches. The trend of converting the electron energy tail into a pair of high-brightness beamlets, capable of producing narrow-band, multi-MeV TS photon signals, is displayed in figure 7.

Figures 7(a.1)–(e.1) permit a few important observations. First, by changing the focusing dynamics of the stack tail, we do not affect electron energy gain. As the electron dephasing is defined by the evolution of the stack head (which remains unchanged), the dephasing is achieved around $z_{\rm deph} = 3.13 \pm 0.05$ mm in all cases, while the mean energy of the leading bunch remains 890 ± 25 MeV. The data in table 1 show that the phase space of the highest-energy e-bunch (I) becomes more compact: in case A4, the energy spread drops from 4% to 2.5%, length by 30% (with a proportional reduction in charge), and emittance by 20% compared to the case A1; hence the increase in 5D brightness to almost 10^{17} A m^{-2}. Yet the spectrum of high-energy γ-photons is only marginally affected (see entries labeled (I) in table 2): the energy spread drops from 19% to 15%, the mean energy staying at 15.6 ± 0.2 MeV. Secondly, replacing the continuous background with a pair of synchronized, fs-length, high-brightness e-bunches completely changes the character of photon emission in the sub-10 MeV range. These bunches, labeled (II) and (III) in table 1, drive TS γ-ray signals containing $(0.4$–$0.9) \times 10^6$ photons with 3–7 MeV mean energy; their spectra are displayed in figures 7(c.2)–(e.2). When the stack tail focusing is the weakest (case A5), electron injection becomes inefficient. This is clear in comparing figures 7(d.1) and (e.1). Even though the photon energy bands in figure 7(e.2) are the most distinct, the reduction in charge of the driving e-beam causes a sharp drop in the photon flux (almost by a factor 2.5 against the case A4). Thus, exceedingly weak focusing in the tail is to be avoided.

4. Optically controlled quasi-monochromatic TS γ-ray pulses

The stacked pulse-driven LPA permits considerable freedom in production of narrow bandwidth γ-ray pulses. We demonstrate this versatility by varying the frequency ratio Ω (from 1.25 to 2) and time delay T (from 0 to

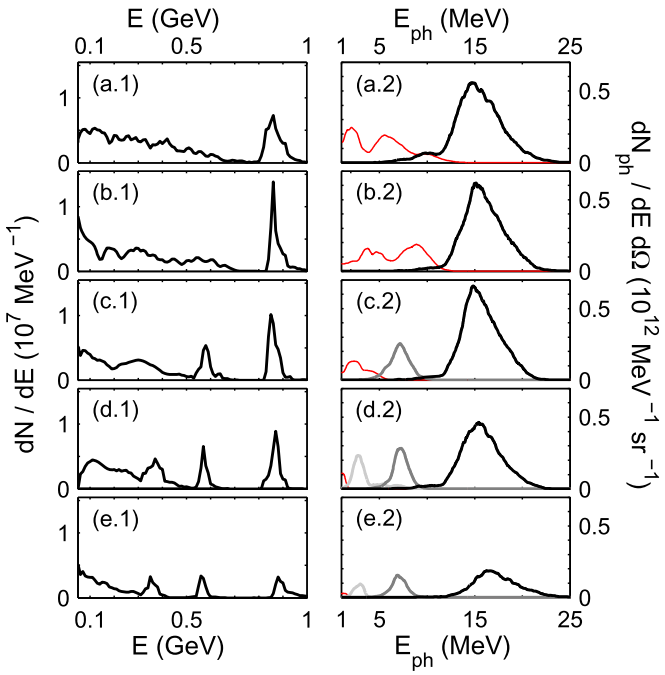

Figure 7. Controlling spectral content of e-beam: from a single e-bunch to the tri-color energy comb. Panels correspond to cases (a) A1, (b) A2, (c) A3, (d) A4, and (e) A5. Left column: electron energy spectra at dephasing. Right column: spectra of TS γ-ray signals from individual QME e-bunches. The spectrum of photons emitted by electrons from the energy tail is depicted with a thin red line. Statistics of QME electron and γ-ray beams are presented in tables 1 and 2.

15 fs) in the stack A2, maintaining spot size matching ($R = 1$) and energy equipartition. Stacks with fully overlapped ($T = 0$) and delayed components ($T = 15$ fs) are considered in sections 4.1 and 4.2. Appendices B and C deal with uneven energy partition in the stack.

4.1. Full overlap of stack components preserves QME acceleration; frequency ratio Ω controls the flux in electron and γ-ray beams

The situation with $T = 0$ differs from the earlier explored regimes [55]. An incoherent mix in the fashion of [67] is not a pulse with a negative step-wise chirp. However, presence of the undelayed $E_{\rm head}$, resilient to self-compression, sufficiently protects the stack from degradation (see figure 8). By changing Ω, one can control the flux dN/dE in the QME e-bunch and, hence, the TS photon yield. To explore the limits of this control, we make a comparative study of three cases:

- Stack B1: $T = 0, R = 1, \Omega = 1.25$;
- Stack B2: $T = 0, R = 1, \Omega = 1.5$;
- Stack B3: $T = 0, R = 1, \Omega = 2$.

Figure 8 demonstrates that increasing Ω from 1.25 to 2 noticeably changes the dynamics of stack degradation. As the components of stacks B1 and B3 plow through the plasma, they both ride on the down-slope of the nonlinear index (such as depicted, e.g. in figure 2 of [10] or figure 7 of [50]); hence a noticeable overall compression of the stack. From figures 8(c) and (d), this compression should be attributed to the degradation of the red component, $E_{\rm tail}$, which red-shifts and compresses to nearly a cycle-long duration. Conversely, as Ω increases, the blue-shifted component becomes more resilient. Figure 8(c) shows that the gently blue-shifted $E_{\rm head}$ of stack B1 is not immune to red-shifting, revealing noticeable compression at the point of electron dephasing. Figure 8(c) also shows that the stack components stay together, accumulating merely a 1.5-cycle delay due to the difference in their group velocities. As the slippage is so small, longitudinal breakup of the stack does not occur, and the stack length remains close to three optical cycles. The stack B3 degrades in a markedly different fashion. From figure 8(d), the second-harmonic $E_{\rm head}$ experiences virtually no erosion, while outrunning the fully compressed first-harmonic $E_{\rm tail}$; the stack starts breaking up. In view of this unfavorable tendency, further increase in Ω is not advisable.

Electron energy spectra at dephasing, with corresponding TS γ-ray signals, are presented in figure 9. Statistics of the QME e-bunches (table 3) and of TS γ-ray pulses (table 4) show the trends in electron and

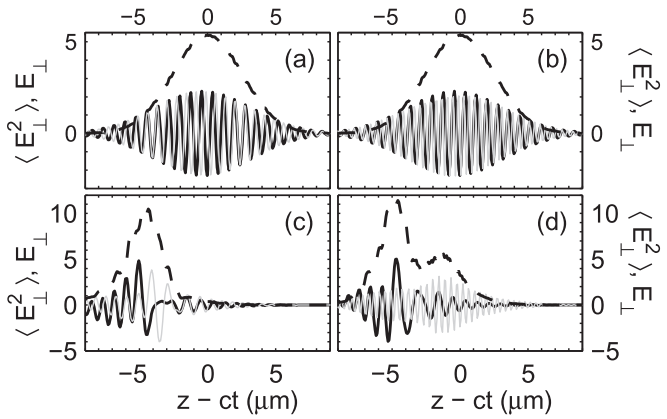

Figure 8. Degradation of the stack with fully overlapped components. The pulses propagate to the right; $z = ct$ is the centroid of the stack in vacuum. Electric field (in units of $m_e\omega_{\rm tail}c/|e|$) is shown on axis. Black: $E_{\rm tail}$; light gray: $E_{\rm head}$ (in the simulation, $\mathbf{E}_{\rm tail} \perp \mathbf{E}_{\rm head}$); dashed curve: $\langle E_\perp^2\rangle = \langle E_{\rm tail}^2\rangle + \langle E_{\rm tail}^2\rangle$, where $\langle\cdots\rangle$ denotes averaging over an optical cycle. Panels (a), (c) correspond to the case B1 ($\Omega = 1.25$), and (b), (d) to the case B3 ($\Omega = 2$). The stack is shown (a), (b) at $z = 0$, and (c), (d) at $z = 2.08$ mm, which is slightly past the point of electron dephasing in the case B1. Presence of the blue-shifted component $E_{\rm head}$ (light gray) prevents self-compression of the stack into a single-cycle optical shock. The stack B3, with a second-harmonic $E_{\rm head}$, shows a tendency to longitudinal breakup (panel (d)).

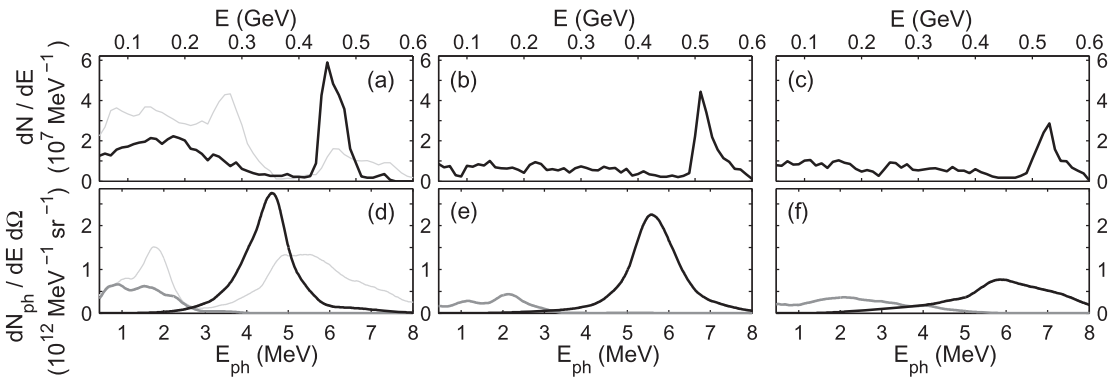

Figure 9. Stacks with fully overlapped components generate QME e-bunches, which, in turn, drive narrow-bandwidth TS γ-ray pulses. Energy spectra of e-beams are shown at dephasing: (a) B1, $z_{\rm deph} \approx 2.03$ mm, (b) B2, $z_{\rm deph} \approx 2.15$ mm, and (c) B3, $z_{\rm deph} \approx 2.47$ mm. The flux in the QME electron signal is boosted compared to the reference signal (light gray in panel (a)), while the background is suppressed. The same tendency holds for the TS γ-rays (energy spectra shown panels (d)–(f)). The QME photon signal (black in panels (d), (e)) is markedly enhanced, while the low-energy tail (gray) is suppressed. Statistics of electron and γ-ray beams are presented in tables 3 and 4.

Table 3. Statistics of QME e-bunches from figures 9(a)–(c). For the sake of convenience, the data on the reference case from table 1 are included.

Parameter	Q	$\langle E\rangle$	σ_E	σ_τ	σ_α	$\varepsilon_\perp^N$	B_n	W
Units	pC	MeV	MeV	fs	mrad	mm mrad	10^{17} A m^{-2}	mJ
Reference	275.0	505.0	45.0	3.40	1.95	0.50	0.66	138.9
B1	392.7	469.8	23.7	4.53	2.90	0.73	0.33	184.5
B2	288.8	524.8	26.3	3.79	2.75	0.64	0.38	151.5
B3	217.0	540.6	25.2	2.93	2.87	0.83	0.22	117.3

Table 4. Statistics of γ-rays emitted by the bunches with parameters from table 3.

Parameter	$\langle E_{\rm ph}\rangle$ (MeV)	σ_E (MeV)	$\Delta\Omega_{\rm ph}$ (μsr)	$N_{\rm ph}$ ($\times 10^6$)	$W_{\rm ph}$ (μJ)
Reference	5.61	1.06	1.61	4.81	4.32
B1	4.56	0.89	1.86	6.72	4.91
B2	5.67	0.97	1.49	5.08	4.61
B3	5.92	1.43	1.40	3.08	2.92

radiation beam production brought about by variation in Ω. Avoiding the buildup of a single-cycle optical shock suppresses continuous injection, while the flux dN/dE in the QME e-bunch receives a considerable boost against the reference case (see figures 9(a)–(c)). Hence the massive increase in the TS photon yield, from comparison of N_{ph} for cases A, table 2, and B, table 4.

Deformation of a stack with fully overlapped components, the process that defines the dephasing length [46, 63], is dominated by rapid self-compression of the least resilient stack component, E_{tail}. In effect, E_{tail} self-compresses (and hence, the stack self-compresses) at the same rate as the drive pulse in the reference scenario [10, 34, 50]. Not surprisingly, as Ω increases from 1.25 to 2, the dephasing length extends by merely 20%, staying close to the dephasing length of the reference case. As a result, the boost in electron and photon energy remains on the same modest scale (see tables 3 and 4). E_{head} of the stack B1, with its modest frequency shift, is not the most efficient protection against the dark current. The energy tail depicted in gray in figure 9(a) contains 880 pC charge, nearly 60% of the tail charge in the reference case. Yet the charge in the QME signal goes up by 50%, and the energy spread drops by half. According to the entry B1 in table 3, this regime is the most energy-efficient among all cases considered in this paper, with 13% of laser energy transferred to the QME e-bunch. The resulting TS γ-ray flux doubles compared to the reference, with a 40% increase in the number of photons.

Early dephasing in case B1 keeps electron energy slightly below the reference level. Increasing Ω pushes electron energy slightly above this level, while virtually eliminating the background. Comparison between figures 9(a) and (b) shows that, in case B2 ($\Omega = 1.5$), the charge in the tail drops by a factor 2.5 against the case B1 ($\Omega = 1.25$), while the charge in QME component is reduced by merely 25%. Consequently, per figure 9(e), emission of the low-energy γ-ray photons is suppressed, while the QME signal, containing roughly 5×10^6 photons with $E_{ph} > 4$ MeV, is not compromised.

As Ω increases further (case B3), the stack tends to break up. The low-energy electron background stays unchanged (see figure 9(c)), while the QME electron signal fades away, loosing 45% of charge against the case B1, also showing emittance degradation. Further reduction of the low-energy photon flux does not occur, while the QME γ-ray signal, depicted in black in figure 9(f), drops nearly three-fold compared to case B1, barely showing above background. Appendix B shows that reducing the energy in the second-harmonic E_{head} improves the e-beam, restoring the γ-ray signal.

4.2. Increasing delay between stack components boosts electron energy

A natural way to control dephasing and, hence, electron energy gain, is to avoid self-compression of E_{tail}, by shifting it deeper into the bubble, away from the longitudinal index gradient in the front of the bubble. In this way, the rigid head of the stack plows through the plasma, driving the wake; and the soft tail controls the bubble radius (thus determining kinetics of self-injection). The advanced in time, blue-shifted E_{head} plays the role of a 'hard hat' placed on top of the vulnerable red-shifted tail [55]. Increasing Ω makes this hard hat more resilient to self-compression. We explore this emerging control option by taking the cases B1–B3 and advancing E_{head} by $T = 15$ fs (same as in section 3). This defines the three new cases:

- Stack C1: $T = 15$ fs, $R = 1, \Omega = 1.25$;
- Stack C2: $T = 15$ fs, $R = 1, \Omega = 1.5$;
- Stack C3: $T = 15$ fs, $R = 1, \Omega = 2$.

Figure 10 demonstrates that the nonzero delay increases resilience of the stack to self-compression. The blue-shifted component E_{head} of the stacks B2 and C2 (both with $\Omega = 1.5$) is almost immune to the red-shift; no sign of its temporal compression is seen in either figure 10(c) or (d). The evolution of E_{tail} turns out to be entirely different. In the case B2, this component rides on the down-slope of the nonlinear index. Figure 10(c) shows that it self-compresses to a cycle-long duration at the same rate as the drive pulse in the reference scenario. In consequence, electrons dephase over the same distance as in the reference case, with virtually no difference in either energy or charge (see entries 'Reference' and B2 in table 3). Conversely, in the case C2, E_{tail} travels inside the evacuated bubble, and thus remains intact (see figure 10(d)). As a result, the stack C2 shrinks very slowly, increasing the dephasing length by 70% against the case B2. The resulting 70% boost in energy can be seen in comparison of figures 9(b) and 11(b). QME e-bunch statistics provided by the entries B2 in table 3 and C2(D) in table 5 reveal a tradeoff between energy gain, charge, and brightness. In the case C2, the increase in energy comes at the expense of a reduction in charge (by a factor 4). This reduction, however, is a consequence of e-bunch shortening, from 3.8 to 0.85 fs. Advancing E_{head} in time merely clips the bunch, almost preserving the mean current (76 and 85 kA in bunches B2 and C2, respectively). The much quieter self-injection in case C2 reduces $\varepsilon_\perp^N$ by a factor 1.6 compared to the case B2, raising the brightness to 1.1×10^{17} A m^{-2}. The entries C2 and C2(D) in table 5 also indicate that $\varepsilon_\perp^N$ is preserved to the third digit as electrons accelerate through dephasing. From the

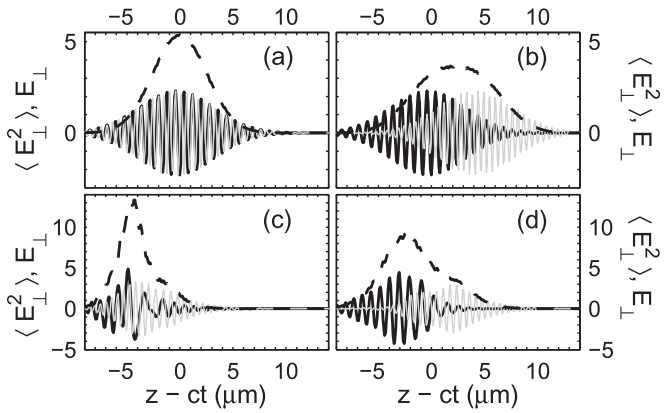

Figure 10. Time delay between stack components makes the stack more resilient to self-compression. Panels (a), (c) correspond to stack B2 (fully overlapped components, $\Omega = 1.5$), and (b), (d) to stack C2 (the head advanced by $T = 15$ fs, $\Omega = 1.5$). The same quantities are shown, and the same gray scale is used, as in figure 8. Stacks are shown (a), (b) at the plasma entrance and (c), (d) at $z = 2.08$ mm, same as in figure 8. Advancing $E_{\rm head}$ in time protects $E_{\rm tail}$ from self-compression, reducing compression of the stack as a whole.

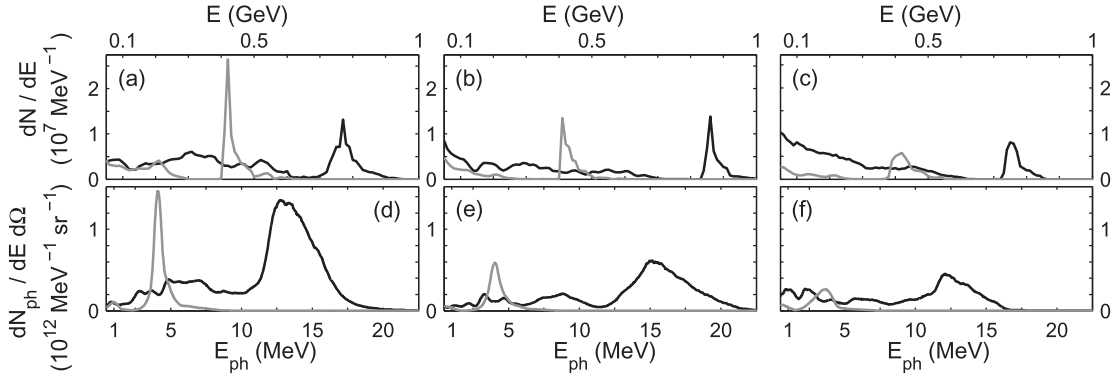

Figure 11. Progress through dephasing of e-beams accelerated with stacks C1–C3 (energy spectra in panels (a)–(c)) and evolution of corresponding TS γ-ray signals (spectra in (d)–(f)). (a), (d) Case C1, $\Omega = 1.25$: e-beam extracted at $z \approx 1.55$ mm (gray) and at dephasing, $z_{\rm deph} \approx 2.95$ mm (black). (b), (e) Case C2, $\Omega = 1.5$: $z \approx 1.47$ mm (gray) and $z_{\rm deph} \approx 3.07$ mm (black). (c), (f) Case C3, $\Omega = 2$: $z \approx 1.51$ mm (gray) and $z_{\rm deph} \approx 2.91$ mm (black). Introducing a 15 fs time delay between stack components boosts electron and photon energy compared to cases with full overlap (see spectra in figure 9). Increasing Ω from 1.25 to 2 marginally affects electron energy gain, while reducing the charge in the QME bunch and the flux in the γ-ray signal. Electron and γ-ray statistics are summed up in tables 5 and 6.

Table 5. Statistics of QME e-bunches from figures 11(a)–(c). The beams at dephasing are labeled (D).

Parameter	Q	$\langle E \rangle$	σ_E	σ_τ	σ_α	$\varepsilon_\perp^N$	B_n	W
Units	pC	MeV	MeV	fs	mrad	mm mrad	10^{17} A m^{-2}	mJ
C1	123.2	448.2	39.2	1.450	2.255	0.346	1.44	55.2
C2	73.13	443.0	31.7	0.845	2.155	0.388	1.16	32.4
C3	67.03	439.7	36.2	0.915	2.560	0.496	0.60	29.5
C1 (D)	123.2	788.5	41.7	1.455	1.200	0.338	1.50	97.1
C2 (D)	73.13	882.0	28.7	0.850	1.350	0.400	1.09	64.5
C3 (D)	67.03	774.2	26.9	0.900	1.785	0.680	0.33	51.9

entries C2 and C2(D) in table 6, tuning the γ-ray energy between 4 and 16 MeV, by extracting the e-bunch before dephasing, conserves the number of photons in the observation cone with the same extraordinary precision. The entries B2 in table 4 and C2(D) in table 6 show that the γ-ray pulse energy content is almost the same, 4.6 and 4.0 μJ, respectively. Hence, even though the number of photons in the pulse C2 is only 30% of $N_{\rm ph}$ in the pulse B2, the power and mean photon energy in the pulse C2 are remarkably higher (4.7 GW against 1.2 GW and 16 MeV against 5.7 MeV).

Table 6. Statistics of γ-rays emitted by the bunches with parameters from table 5.

Parameter	$\langle E_{ph}\rangle$ (MeV)	σ_E (MeV)	$\Delta\Omega_{ph}$ (μsr)	N_{ph} ($\times 10^6$)	W_{ph} (μJ)
C1	4.42	0.92	2.04	2.85	2.02
C2	4.36	0.93	2.09	1.50	1.05
C3	3.61	0.96	2.12	0.98	0.57
C1 (D)	13.8	2.275	0.66	3.77	8.32
C2 (D)	16.0	2.506	0.53	1.56	4.00
C3 (D)	12.2	2.660	0.68	1.28	2.51

A comparison of electron spectra in figures 9 and 11 and data in tables 3 and 5 reveals that advancing the stack head increases electron energy by 70% in cases C1 and C2, and by 40% in the less optimal case C3 compared to their respective counterparts B1–B3. However, as soon as T is fixed at 15 fs, electron energy becomes almost insensitive to Ω, varying by ≈10% as Ω grows from 1.25 to 2, while the charge in the bunch gradually drops (see entries C1(D)–C3(D) in table 5). The same trend was observed earlier for the cases with zero delay (section 4.1). This trend notwithstanding, the stacks C1 ($\Omega = 1.25$) and C2 ($\Omega = 1.5$) both generate ultra-bright 85 kA e-bunches, emitting the TS γ-ray pulses with a power of 5.7 and 4.7 GW, mean energy $\langle E_{ph}\rangle \approx 14$ and 16 MeV, respectively, and ≈16% energy spread. Yet, the 4-fold reduction in the e-bunch charge in the case C2 reduces the number of γ-photons by a factor 2.5. Similarly to the case of zero delay, the e-bunch emittance and the TS signal degrade for $\Omega = 2$ (case C3). Indeed, e-beams accelerated through dephasing in cases C2 and C3 produce almost the same level of low-energy photon signal ($E_{ph} < 10$ MeV in figures 11(e) and (f)), while the useful QME part of the C3 photon spectrum fades away.

4.3. All-optical control of quasi-monochromatic TS γ-ray sources: concluding remarks

Judicious variation of the stack components permits precise all-optical control of electron injection and acceleration processes. Thereby, the phase space of the QME e-bunch may be tailored to achieve the desired parameters of quasi-monochromatic γ-ray pulses. It is shown that the QME e-bunches, coming from the stacked pulse-driven LPA, carry charge from 70 to almost 400 pC; their duration (and hence duration of the TS γ-ray pulses) ranges from 0.85 to 4.5 fs, and the 5D brightness from $\approx 2 \times 10^{16}$ to 2×10^{17} A m^{-2}. In all cases, the low-energy background remains sufficiently suppressed, both in electron and TS γ-ray signals. The main trends in electron and photon beam manipulation may be summed up as follows.

(i) As long as the time delay (T) and energy partition between the stack components are fixed and $\Omega \geqslant 1.25$, the electron energy gain is quite insensitive to the frequency ratio. The peak flux dN/dE in the QME e-bunch, however, drops as Ω increases. Emittance and brightness of the bunch degrade as $\Omega \to 2$, bringing noticeable reduction in the quasi-monochromatic TS γ-ray signal.

(ii) Stacks with fully overlapped components boost the peak flux in the QME e-bunch most efficiently, while keeping electron energy at the reference level (≈500 MeV), and the 5D brightness at $\approx 3 \times 10^{16}$ A m^{-2}. For $\Omega \leqslant 1.5$, the low-energy background is suppressed so remarkably as to keep the average flux of low-energy photons under 15% of the peak flux, the quasi-monochromatic γ-ray signal containing $\approx 6 \times 10^6$ photons with $\langle E_{ph}\rangle \approx 5$ MeV.

(iii) Advancing the blue-shifted stack component by $T \sim \tau_L$, while keeping Ω fixed, boosts electron energy. For a stack with $\Omega \leqslant 1.5$, the electron energy increases, on average, from ≈500 to ≈850 MeV, at the expense of reduction in charge and peak flux in the QME bunch. As no reduction in current occurs, while much quieter injection reduces the emittance, the 5D brightness of the bunch is pushed above 10^{17} A m^{-2}. The resulting 5 GW γ-ray pulses contain over 1.5×10^6 photons, with $\langle E_{ph}\rangle \approx 15$ MeV and ≈16% energy spread.

Point (i) permits a considerable technological flexibility in a practical realization of this concept. Frequency shifting on the modest scale ($\Omega \leqslant 1.5$) can be accomplished with a Raman cell, with subsequent conventional chirped-pulse amplification [68–70]. Alternatively, energy-efficient methods of frequency-doubling of the primary pulse may be applied. In the latter case, it is important to remember that, even though the resulting e-bunch is not as good a driver of a quasi-monochromatic TS signal, this signal still has a quality far exceeding that accessible in the reference scenario.

Perfect alignment of stack components is of paramount importance. Alignment of their propagation axes as well as minimal radial mismatch of centroids is necessary to avoid transverse breakup of the driver and the e-beam [71, 72] or the 'wiggling' of the bubble and the e-beam centroid [73]. Real-time optimization made possible with a kHz-scale repetition rate [58, 59] is instrumental to meeting this challenge.

Lastly, the parameters of our exploratory, proof-of-principle simulations were not chosen with any specific experimental proposal in mind, even though sub-Joule energy, 20–30 fs drive pulses, as well as 2–3 mm length dense gas-jet targets are typical of most laboratories pursuing research in LPA-based light sources. The data on the TS γ-ray yield, which is in the range of a few 10^6 quasi-monochromatic photons per shot, must be thus regarded as a reference, aiming to learn the trends in the γ-ray pulse variations brought about by the changes in optically controlled e-beam phase space. As soon as the trends are made clear, there are a number of technological options to bring the energy or the photon yield up, to satisfy the demands of applications. Increase in the photon energy beyond the demonstrated 15 MeV may be accomplished by substantially increasing the ILP frequency [44]. Additionally, using an order-of-magnitude longer (up to 2.5 ps) ILP of the same amplitude, $a_{\rm int} = 0.1$, should proportionally increase the photon yield, raising the photon number from a few 10^6 to a few 10^7 per shot. This would require quarter-Joule ILP energy, which is still below the LPA drive pulse energy, and thus should not preclude matching the repetition rates of the LPA and the ILP. The half-length of the 2.5 ps ILP is one-third of its Rayleigh length, sufficient to preserve the almost planar-wave character of the ILP as it interacts with the e-bunch. A very limited energy in the LPA drive pulse and the ILP permits increasing the repetition rate of the γ-ray source towards hundreds of Hz. This can be afforded with a kW-scale average power amplifier, a hard yet practical task [74]. This increase in the repetition rate should further boost the photon yield by two to three orders of magnitude. All in all, the proposed TS-based source, using a 10 TW scale, stacked pulse-driven LPA, promises to generate over 10^9 quasi-monochromatic photons per second, with their mean energy tunable up to 15 MeV (and beyond), a clear alternative to using one-per-hour repetition rate PW facilities [45]. It should be noted that simulations, based on the data of recent detection experiment [21], indicate that the TS γ-ray flux of 10^6 photons per second, with a 5% TS signal bandwidth and a 10 Hz repetition rate, is sufficient to identify a nuclear resonance fluorescence peak from a 1 kg of highly enriched uranium within 10 min. Raising the repetition rate by three orders of magnitude, even with the bandwidth up to a factor 4 higher, is thus promising for the design of nondestructive inspection systems for special nuclear materials. Reduction in the photon energy spread from the demonstrated 15% may be pursued through frequency chirping of the ILP [7]. Given the genuine unconventional U-shape of momentum chirp in the QME e-bunch (see figures 3(a) and 6(a)), this topic deserves special consideration and is left for future publications.

5. Summary and outlook

In a conventional LPA, electrons self-injected from the ambient plasma are accelerated in the plasma wake bucket—a cavity of electron density maintained by the radiation pressure of a single narrow-bandwidth laser pulse. Deformations of the bucket, which carry on in a lock-step with the deformations of the optical driver, determine the structure of the e-beam phase space. Optimizing the nonlinear evolution of the drive pulse, through photon engineering, is a vital element of LPA design, offering new avenues to coherently control e-beam phase space on the femtosecond scale.

Compact sources of QME γ-photons, based on the TS mechanism, are highly sensitive to the quality and phase space structure of the driving GeV-scale e-beams. Reaching sufficient e-beam brightness and energy, while maintaining a modest facility footprint and high repetition rate, is a major challenge for a traditional LPA. The first road block is the limit on electron energy imposed by dephasing, with unavoidable beam contamination with a low-energy background, while the second is the low repetition rate of PW-scale lasers (which limits the dosage, frustrating applications). Reducing the energy in the drive pulse to a sub-Joule level may alleviate the latter, yet aggravating the former. Our simulations show that the resolution of this conflict may be found in synthesizing the LPA drive pulse by incoherently stacking collinearly propagating 10 TW-scale pulses of different wavelengths, with the blue-shifted pulse advanced in time [55]. This stacking emulates a step-wise negative frequency chirp, with a frequency bandwidth sufficient to compensate the red-shift imparted by the wake excitation. Unlike a single, transform-limited pulse, the stack is well protected from degradation while driving the bubble in a dense plasma ($n_0 \sim 10^{19}$ cm^{-3}). This delays electron dephasing, almost doubling the electron energy compared to the limits of accepted scalings, using no manipulations of a few mm length, flat gas jet target. And, immunity of the stacked driver to self-compression keeps the low-energy electron flux so modest as to almost avoid contamination of TS γ-ray pulse with low-energy photons.

Simulation data presented here reveal remarkable versatility of the stacked pulse-driven LPA in all-optical control over the e-bunch phase space. The frequency difference between the stack components controls the electron flux dN/dE, thus controlling the photon yield, while the delay between the components controls the energy gain. (Changing the energy partition in the stacked driver is another degree of freedom.) This way, emission of more than 10^6 quasi-monochromatic photons per shot, affording kHz-scale repetition rate, with the mean energy tunable up to 15 MeV (which is in the range of interest for nuclear photonics [8]), appears to be within reach of existing laser technology. We further show that trains of synchronized, high-brightness

GeV-scale e-bunches of different energies may be produced in a single shot. Generation of these unconventional beams, inaccessible with standard acceleration techniques, is achieved by weak focusing of the trailing component of the stack. Induced periodic focusing in the stack tail enforces oscillations in the bubble size, similarly to the effect earlier observed in the plasma channels [9, 10, 55]. The resulting periodic injection generates a background-free bunch train that emits up to 3×10^6 photons into a μsr-scale observation solid angle. The photons are distributed among two or three well resolved spectral bands, in the range 3–17 MeV. By selectively focusing e-bunches of different energies with highly chromatic magnetic quadrupole lenses [75, 76] before the collision point, one can further control the output of the TS source, selectively suppressing or enhancing the brightness of different γ-ray beamlets. The natural mutual synchronization of fs-length e-bunches and γ-ray pulses may be an asset to nuclear pump-probe experiments. With a γ-ray beam spectrally resolved, each beamlet may give a 'movie frame' on a femtosecond time scale to image ultrafast phenomena in a dense matter [22].

Acknowledgments

Work of SYK and BAS has been supported by the National Science Foundation Grant PHY-1535678. TS simulations were completed utilizing the Holland Computing Center (HCC) of the University of Nebraska. SYK expresses his cordial gratitude to Natasha Pavlovikj for her assistance in using the high-performance computing resources at HCC.

Appendix A. Spectral properties of photons emitted by an e-beam with large divergence

The geometry of TS from a single electron is presented in figure A1. The electron trajectory is defined by the polar θ_e and azimuthal ϕ_e incidence angles, while the detector is placed along the line defined by the polar and azimuthal angles θ and ϕ. In the limit of small-angle scattering, $\theta \sim \theta_e \ll \pi$, the photon energy is given by a known formula [5]

$$E_{\rm ph} = \frac{4\gamma_e^2 E_{\rm int}}{1 + \gamma_e^2((\theta - \theta_e)^2 + 4\theta_e\theta \sin^2((\phi - \phi_e)/2))}. \tag{A.1}$$

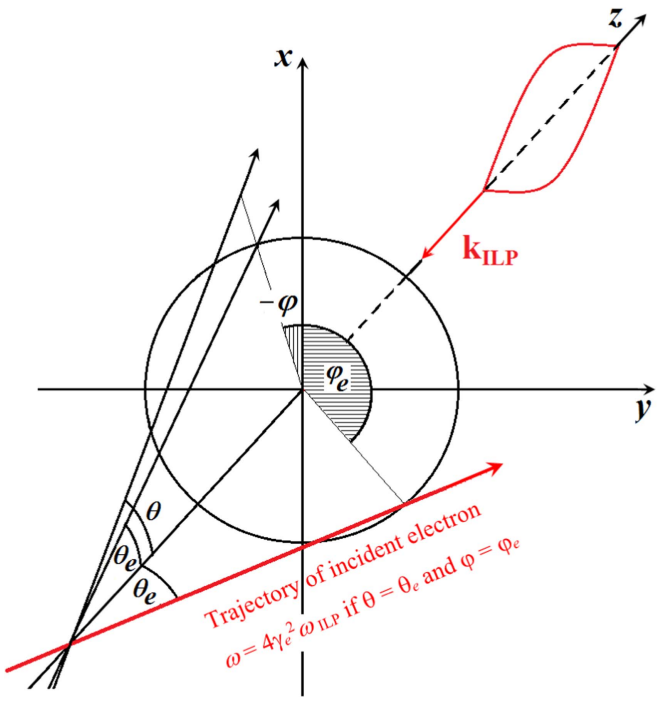

Figure A1. Geometry of near-backward TS. The ILP (with a wave vector $\mathbf{k}_{\rm ILP} = -\mathbf{e}_z k_{\rm ILP}$) propagates in the negative z direction. Electron trajectory is characterized by polar θ_e and azimuthal ϕ_e incidence angles. When the observation and incidence polar angles θ and θ_e are small, the highest photon energy corresponds to scattering along the incident electron trajectory ($\theta = \theta_e, \phi = \phi_e$).

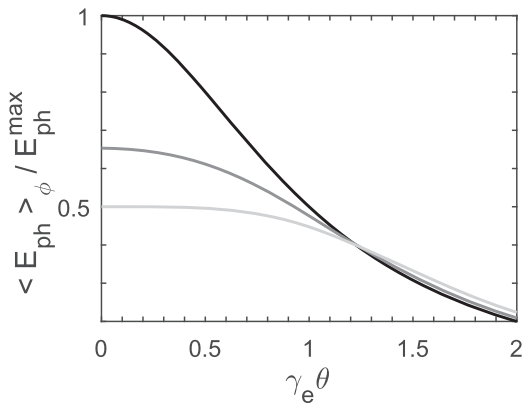

Figure A2. Average energy of photons (A.2) scattered from electrons incident at an angle $\theta_e = 0$ (black), $2^{-1/2}\gamma_e^{-1}$ (dark gray), and γ_e^{-1} (gray). Photon energy remains almost flat for $\theta < \theta_e$, and decays for $\theta > \gamma_e^{-1}$ at a rate that is weakly sensitive to θ_e.

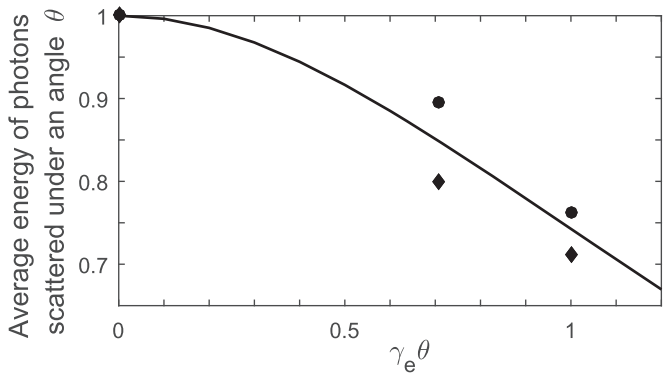

Figure A3. Normalized average energy of photons (A.5) versus detection angle. Averaging is made over the azimuthal angle and over the interval $0 \leqslant \theta_e \leqslant 2\gamma_e^{-1}$ of electron incidence angles. Markers correspond to normalized photon energies averaged over the distributions shown in figures 3(c) and (d). Difference between round markers (scattering in the ILP polarization plane), and diamonds (scattering in the orthogonal plane) are due to a slight asymmetry of electron distribution in the realistic simulation.

If the detector is aligned with the incident electron trajectory, $\theta = \theta_e$, $\phi = \phi_e$, the photon energy has a global maximum $E_{\rm ph} = E_{\rm ph}^{\rm max} = 4\gamma_e^2 E_{\rm int}$ *regardless of the incidence angles*. Photons scattered under an angle θ in the electron incidence plane, $\phi = \phi_e$, have their energy reduced against $E_{\rm ph}^{\rm max}$ by a factor $(1 + \gamma_e^2(\theta - \theta_e)^2)^{-1}$.

The electron distribution in the transverse phase space (x, y, p_x, p_y) determines flux and energy of γ-photons scattered at small angles. If the electron momentum distribution is independent of azimuthal angle, the energy of photons emitted in the given direction may be evaluated by averaging the spectrum (A.1) over $\varphi = \phi - \phi_e$:

$$\langle E_{\rm ph}\rangle_\varphi = \frac{1}{\pi}\int_0^\pi E_{\rm ph}\,{\rm d}\varphi = \frac{E_{\rm ph}^{\rm max}}{\sqrt{(1+\gamma_e^2(\theta-\theta_e)^2)(1+\gamma_e^2(\theta+\theta_e)^2)}}. \tag{A.2}$$

Dependence (A.2) is shown in figure A2. For the direct backscattering from an electron propagating along the z-axis, $\theta = \theta_e = 0$, equation (A.2) yields $E_{\rm ph} = E_{\rm ph}^{\rm max}$. For scattering from electrons aligned along the cone with an opening angle θ_e, as shown in figure A1, we have

$$\langle E_{\rm ph}\rangle_\varphi(\theta = \theta_e) = E_{\rm ph}^{\rm max}(1 + 4\gamma_e^2\theta_e^2)^{-1/2}. \tag{A.3}$$

For $\theta_e = \sigma_\alpha \approx 2.75\gamma_e^{-1}$, $\gamma_e = 1705$, and $E_{\rm int} = 1.5$ eV, as in the case discussed in section 3.2, the estimate (A.3) yields the reduction in the mean energy of photons by a factor 0.18. This is consistent with the mean energy of simulated TS spectra in figures 3(c) and (d) (red curves).

If the beam is weakly collimated, so that $\theta_e \approx \sigma_\alpha \gg \gamma_e^{-1}$, reduction in photon energy for the scattering under small angles, $\theta \sim \gamma_e^{-1}$, may be estimated, using (A.2), as

$$\langle E_{\rm ph}\rangle_\varphi(\theta \ll \theta_e,\ \theta_e) \approx \langle E_{\rm ph}\rangle_\varphi(0,\ \theta_e) + \frac{\theta^2}{2}\frac{\partial^2\langle E_{\rm ph}\rangle_\varphi}{\partial\theta^2}\bigg|_{\theta=0}$$
$$= \frac{E_{\rm ph}^{\rm max}}{1+(\gamma_e\theta_e)^2}\left(1 - \frac{(\gamma_e\theta)^2}{1+(\gamma_e\theta_e)^2}\right). \quad (A.4)$$

If we set $\theta_e = \sigma_\alpha \approx 2.75\gamma_e^{-1}$, as in the case discussed in section 3.2, equation (A.4) gives $\langle E_{\rm ph}\rangle_\varphi(\theta) \approx 0.12E_{\rm ph}^{\rm max}(1 - 0.34\theta^2$ (mrad)). The estimates (A.3) and (A.4) thus indicate that, regardless of the detection angle, electrons incident at an angle $\theta_e \sim \sigma_\alpha \gg \gamma_e^{-1}$ do not contribute to the high-energy part of photon spectrum.

For weakly collimated beams, electrons fill the region of phase space corresponding to small incidence angles, $\theta_e \sim \gamma_e^{-1} \ll \sigma_\alpha$, almost uniformly. Hence, the reduction in photon energy with an increase in the detection angle θ may be estimated by averaging the distribution (A.2) over θ_e, in the interval $[0,\ 2\gamma_e^{-1}]$:

$$\tilde{E}_{\rm ph}(\theta) = \frac{\langle E_{\rm ph}\rangle_{\varphi,\theta_e}(\theta)}{\langle E_{\rm ph}\rangle_{\varphi,\theta_e}(0)} = \frac{\int_0^{2/\gamma_e}\langle E_{\rm ph}(\theta)\rangle_\varphi\ {\rm d}\theta_e}{\int_0^{2/\gamma_e}\langle E_{\rm ph}(0)\rangle_\varphi\ {\rm d}\theta_e}, \quad (A.5)$$

where the normalization factor corresponds to the direct backscattering. Changing the averaging interval weakly affects $\tilde{E}_{\rm ph}(\theta)$ for $0 < \theta < \gamma_e^{-1}$. Even though all our estimates implied the lack of correlation between the electron energy and transverse momentum, also ignoring the fact that most electrons propagate off-axis, figure A3 shows that the normalized average energy (A.5) agrees well with results of first-principle simulations.

Appendix B. Stack with fully overlapped first- and second-harmonic components: reducing second-harmonic energy improves e-beam, restoring narrow-bandwidth TS γ-ray signal

It was established in section 4.1 that the stack of fully overlapped, same-energy first- and second-harmonic components (B3) breaks up before electron dephasing, generating an e-beam that performs poorly as a TS driver. Reducing the second-harmonic energy mitigates the effect of breakup. From figures B1(a), (b) and table B1, reducing the second-harmonic energy from 0.7 J (case B3) to 0.35 J (case $B3_{(1:2)}$) and, further, to 0.175 J (case $B3_{(1:4)}$) results in ≈20% reduction in the mean electron energy, while the energy spread stays below 5%, and the emittance drops by ≈20%. At the same time, the flux in the low-energy tail does not go up. Thus, addition of a 100 mJ-scale, second-harmonic component to a Joule-scale first-harmonic drive pulse saves QME e-beam from degradation. Equally interesting, figures B1(c) and (d) show that the low-energy background in e-beams, generated with stacks $B3_{(1:2)}$ and $B3_{(1:4)}$, makes less contamination of the TS γ-ray spectra than in the case B3.

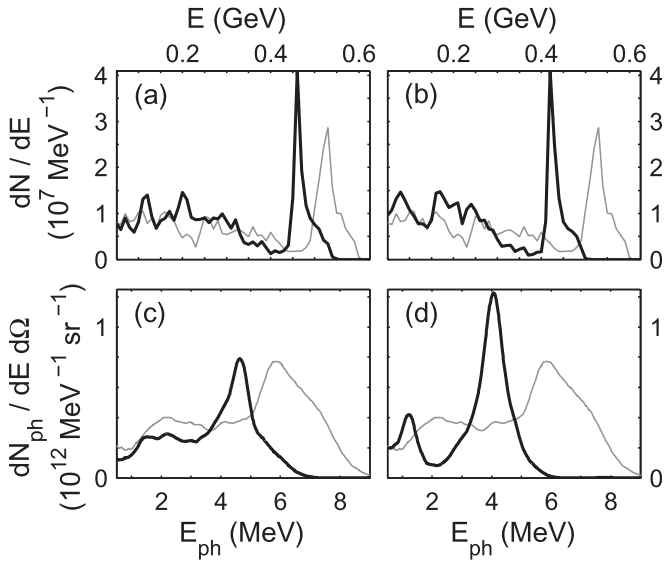

Figure B1. Stacks with fully overlapped first- and second-harmonic components, with the second-harmonic energy reduced (a), (c) by 50% (case $B3_{(1:2)}$), and (b), (d) by a factor 4 (case $B3_{(1:4)}$), sustain quasi-monoenergetic electron acceleration. Low-energy background in electron spectra at dephasing ((a) $z_{\rm deph} \approx 2.19$ mm, (b) $z_{\rm deph} \approx 2.31$ mm) remains as weak as in the case of energy equipartition (B3, gray), the QME components having higher flux and lower energy spread. In contrast to case B3 (light gray), QME γ-ray signals become distinct against the background (black in (c), (d)). Electron and photon statistics are presented in tables B1 and B2.

Table B1. Statistics of QME e-bunches from figures 9(c), B1(a) and (b).

Parameter Units	Q pC	$\langle E\rangle$ MeV	σ_E MeV	σ_τ fs	σ_α mrad	$\varepsilon_\perp^N$ mm mrad	B_n 10^{17} A m^{-2}	W mJ
B3	217.0	540.6	25.2	2.93	2.87	0.83	0.22	117.3
B3$_{(1:2)}$	191.8	471.4	23.5	2.67	3.26	0.71	0.29	90.4
B3$_{(1:4)}$	186.5	441.7	21.0	2.62	2.90	0.65	0.34	82.4

Table B2. Statistics of γ-rays emitted by the bunches with parameters from table B1.

Parameter	$\langle E_{\rm ph}\rangle$ (MeV)	σ_E (MeV)	$\Delta\Omega_{\rm ph}$ (μsr)	$N_{\rm ph}$ ($\times 10^6$)	$W_{\rm ph}$ (μJ)
B3	5.92	1.43	1.40	3.08	2.92
B3$_{(1:2)}$	4.39	1.05	1.85	2.50	1.76
B3$_{(1:4)}$	4.06	0.71	2.10	3.06	2.00

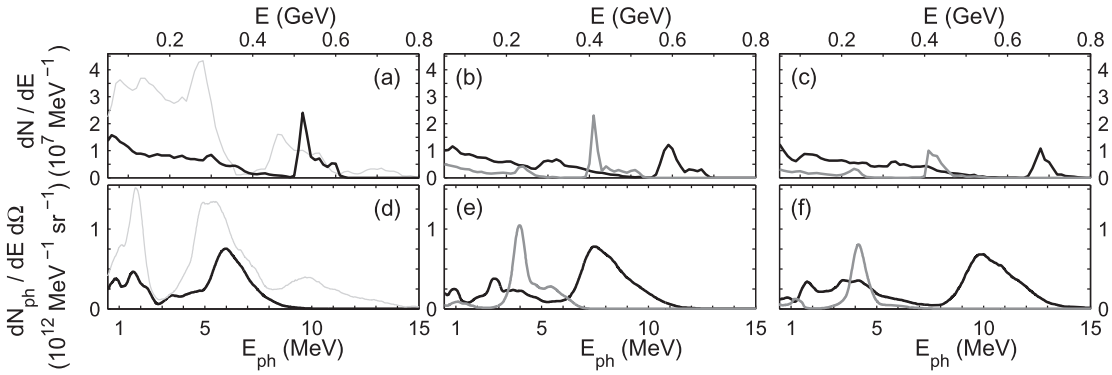

Figure C1. Increasing time delay between the stack components boosts the energy of electrons (spectra in (a)–(c)) and TS γ-photons (spectra in (d)–(f)). Electrons are accelerated with the stacks S-A1$_{(4:9)}$–S-A3$_{(4:9)}$, having $\Omega = 1.5$ and reduced energy in the head component. (a), (d) S-A1$_{(4:9)}$: electrons are extracted at dephasing, $z_{\rm deph} \approx 2.31$ mm (black); the reference case: $z_{\rm deph} \approx 2.11$ mm (light gray, same as in figure 2). (b), (e) S-A2$_{(4:9)}$: $z \approx 1.63$ mm (gray), $z_{\rm deph} \approx 2.43$ mm (black). (c), (f) S-A3$_{(4:9)}$: $z \approx 1.55$ mm (gray), $z_{\rm deph} \approx 2.67$ mm (black). Electron and γ-ray statistics are shown in tables C1 and C2. Uneven energy partition in the stack does not compromise low level of background in both electron and TS γ-ray signals.

And, case B3$_{(1:4)}$ demonstrates a 50% boost in the peak photon flux. As the QME γ-ray signals become more distinct against the background, their central energy drops from roughly 6 to 4 MeV, while the photon yield shown in Table B2 changes insignificantly. With this compromise in mind, a judicious choice of energy partition between the stack components markedly improves generation of QME e-bunches, making them suitable drivers of narrow-bandwidth TS γ-ray sources.

Appendix C. Stack with reduced-energy head: increasing delay between head and tail boosts electron energy

As discussed in section 4, increasing the time delay between the stack components increases the energy and brightness of the QME e-bunches. Implementation of this scheme, however, is likely to be hampered by the technical difficulty of generating sufficient frequency shift in the pulse, while maintaining Joule-scale energy and high optical quality. To show that the acceleration process is exceptionally tolerant to energy fluctuations in the stack components, we modify the stacks S-A1–S-A3 of [55] by reducing the energy in their heads by a factor 2.25 (from 0.7 to 0.311 J), so that $\mathcal{E}_{\rm head} = (2/3)\,\mathcal{E}_{\rm tail} = 1.54$. The three resulting stacks are as follows:

- Stack S-A1$_{(4:9)}$: $\Omega = 1.5, R = 1, T = 10$ fs;
- Stack S-A2$_{(4:9)}$: $\Omega = 1.5, R = 1, T = 15$ fs;
- Stack S-A3$_{(4:9)}$: $\Omega = 1.5, R = 1, T = 20$ fs.

Table C1. Statistics of QME e-bunches at dephasing from figures C1(a)–(c).

Parameter Units	Q pC	$\langle E\rangle$ MeV	σ_E MeV	σ_τ fs	σ_α mrad	$\varepsilon_\perp^N$ mm mrad	B_n 10^{17} A m^{-2}	W mJ
S-A1$_{(4:9)}$	151.4	548.3	28.2	2.23	2.63	0.54	0.47	83.0
S-A2$_{(4:9)}$	104.8	612.8	30.2	1.51	1.65	0.31	1.49	64.2
S-A3$_{(4:9)}$	67.83	694.3	21.7	1.04	1.22	0.26	1.96	47.1

Table C2. Statistics of γ-rays emitted by the bunches with parameters from table C1.

Parameter	$\langle E_{\rm ph}\rangle$ (MeV)	σ_E (MeV)	$\Delta\Omega_{\rm ph}$ (μsr)	$N_{\rm ph}$ ($\times 10^6$)	$W_{\rm ph}$ (μJ)
S-A1$_{(4:9)}$	6.23	1.16	1.36	2.19	2.18
S-A2$_{(4:9)}$	8.13	1.38	1.09	2.23	2.90
S-A3$_{(4:9)}$	10.5	1.48	0.85	1.68	2.82

The index '(4:9)' stands for the energy partition between the head and the tail. Electron energy spectra before and at dephasing, with the corresponding TS γ-ray signals, are presented in figure C1. Statistics of QME electron and TS γ-ray beams are summed up in tables C1 and C2.

Lower energy in the stack head brings one benefit. In the case S-A3 (energy equipartition), the e-beam was lost due to inefficient injection [55]. Reducing the energy in the head (case S-A3$_{(4:9)}$) brings the beam back (see figure C1(c) and entry S-A3$_{(4:9)}$ in table C1), the highest-energy and the brightest one among the three reduced-energy cases. This QME e-bunch emits a 2.7 GW photon pulse with 10.5 MeV mean energy and 14% energy spread (the lowest among all considered cases), well separated from the background (see figure C1(f)).

Altogether, the QME e-bunches at dephasing are of excellent quality. For every 5 fs increase in T, their mean energy receives an increment of roughly 75 MeV, while the charge drops by $\approx$42 pC. In cases S-A1$_{(4:9)}$ and S-A2$_{(4:9)}$ this reduction in charge comes with a proportional reduction in the bunch length, so that the mean current remains 68 kA (in case S-A3$_{(4:9)}$ it drops to 55 kA). The normalized transverse emitance also drops by more than half, reaching 0.26 mm mrad in case S-A3$_{(4:9)}$, the lowest among all cases studied in this paper. Not surprisingly, the brightness of the bunches quadruples, from $\approx 5 \times 10^{16}$ in case S-A1$_{(4:9)}$ to $\approx 2 \times 10^{17}$ A m^{-2} in case S-A3$_{(4:9)}$. This makes them perfect TS drivers. From figures C1(d)–(f) and table C2, as the mean photon energy increases from 6.2 to 10.5 MeV and the power in the signal from 1 to 2.7 GW (the energy spread dropping from 18.5% to 14%), the peak flux in the photon signal remains almost unchanged at 8×10^{11} MeV^{-1} sr^{-1}, while the number of photons stays at the 2×10^6 level.

Returning to section 4.2, recalling the data on electron acceleration and photon production in the case C2 (equivalent to the case S-A2 of [55]), and comparing them with the data pertaining to the case S-A2$_{(4:9)}$, we observe the changes in the QME electron and photon signals. First, the mean electron energy in case S-A2$_{(4:9)}$ drops by a factor 0.7 compared to the case C2/S-A2, while the normalized transverse emittance drops by a factor of 0.775. The energy spread, on the other hand, increases from 3.25% to 4.9%. Hence the brightness of the QME bunch S-A2$_{(4:9)}$ increases compared to cases C2/S-A2 by a factor of 1.35, reaching 1.5×10^{17} A m^{-2}. Comparison of figures 11(e) and C1(e) tells us that the peak photon flux does not change as the aforementioned changes in the e-bunch take place. Although the central energy in the γ-ray signal drops by half, the energy spread remains at 16%. Even though the number of photons in case S-A2$_{(4:9)}$ is about 1.4 times higher, lower photon energy and shorter pulse duration cause the drop in power, from 4.7 to 1.9 GW. The next important observation is the increased level of low-energy electron background in cases S-A1$_{(4:9)}$–S-A3$_{(4:9)}$, owing to more rapid degradation of the stacks with the reduced-energy head. The tails in figures C1(a)–(c) are very similar, containing, on average, 460 pC charge. In cases S-A1$_{(4:9)}$ and S-A2$_{(4:9)}$, this indicates a factor 1.35 and 1.8 increase compared to cases S-A1 and C2/S-A2 [55]. Yet, even though the flux of low-energy photons in case S-A2$_{(4:9)}$ (figure C1(e)) doubles compared to the flux in the C2/S-A2 case (figure 11(e)), the high-energy, QME photon signal remains very distinct.

In summary, a decrease in the stack head energy by more than 50% does not degrade the average characteristics of the QME e-beams. These remain perfectly suitable to generate narrow-bandwidth, GW-scale γ-ray pulses containing 10^6 photons with the mean energy up to 10 MeV. An increase in the low-energy photon background ($E_{\rm ph} < 5$ MeV) is not a major impediment; the source of this contaminant, the weak continuous low-energy background in the e-beam, may be dispersed in the magnetic spectrometer [75, 76] before the interaction with ILP. In conclusion, even though reducing the energy in the stack head reduces the window of accessible electron and photon beam parameters, the e-beam control can be exercised even in these more limited circumstances.

ORCID iDs

S Y Kalmykov https://orcid.org/0000-0002-0946-857X

References

[1] Sarachik E S and Schappert G T 1970 *Phys. Rev.* D **1** 2738
[2] Esarey E, Ride S K and Sprangle P 1993 *Phys. Rev.* E **48** 3003
[3] Ride S K, Esarey E and Baine M 1995 *Phys. Rev.* E **52** 5425
[4] Lau Y Y, Fei H, Umstadter D P and Kowalczyk R 2003 *Phys. Plasmas* **10** 2155
[5] Tomassini P, Giulietti A, Giulietti D and Gizzi L A 2005 *Appl. Phys.* B **80** 419
[6] Albert F, Anderson S G, Gibson D J, Marsh R A, Wu S S, Siders C W, Barty C P J and Hartemann F V 2011 *Phys. Rev. Accel. Beams* **14** 050703
[7] Ghebregziabher I A, Shadwick B A and Umstadter D P 2013 *Phys. Rev. Spec. Top. Accel. Beams* **16** 030705
[8] Rykovanov S G, Geddes C G R, Vay J-L, Schroeder C B, Esarey E and Leemans W P 2014 *J. Phys. B: At. Mol. Opt. Phys.* **47** 234013
[9] Kalmykov S Y, Davoine X, Ghebregziabher I, Lehe R, Lifschitz A F and Shadwick B A 2016 *Plasma Phys. Control. Fusion* **58** 034006
[10] Kalmykov S Y, Davoine X, Ghebregziabher I and Shadwick B A 2016 *Nucl. Instrum. Methods Phys. Res.* A **829** 52
[11] Kalmykov S Y, Davoine X, Ghebregziabher I and Shadwick B A 2017 *AIP Conf. Proc.* **1812** 100001
[12] Hsu I C, Chu C C and Yu C I 1996 *Phys. Rev.* E **54** 5657
[13] Baylac M *et al* 2002 *Phys. Lett.* B **539** 8
[14] Sakai I *et al* 2003 *Phys. Rev. Accel. Beams* **6** 091001
[15] Omori T *et al* 2006 *Phys. Rev. Lett.* **96** 114801
[16] Kawase K, Arimoto Y, Fujiwara M, Okajima S, Shoji M, Suzuki S, Tamura K, Yorita T and Ohkuma H 2008 *Nucl. Instrum. Methods Phys. Res.* A **592** 154
[17] Kikuzawa N, Hajima R, Nishimori N, Minehara E, Hayakawa T, Shizuma T, Toyokawa H and Ohgaki H 2009 *Appl. Phys. Express* **2** 036502
[18] Hayakawa T, Ohgaki H, Shizuma T, Hajima R, Kikuzawa N, Minehara E, Kii T and Toyokawa H 2009 *Rev. Sci. Instrum.* **80** 045110
[19] Albert F *et al* 2010 *Phys. Rev. Accel. Beams* **13** 070704
[20] Jochmann A *et al* 2013 *Phys. Rev. Lett.* **111** 114803
[21] Ohgaki H *et al* 2017 *IEEE Trans. Nucl. Sci.* **64** 1635
[22] Scoby C M 2013 Adapting high brightness relativistic electron beams for ultrafast science *PhD Thesis* The University of Caifornia, Los Angeles (http://escholarship.org/uc/item/11p8s2h1)
[23] Esarey E, Schroeder C B and Leemans W P 2009 *Rev. Mod. Phys.* **81** 1229
[24] Malka V 2012 *Phys. Plasmas* **19** 055501
[25] Lundh O *et al* 2011 *Nat. Phys.* **7** 219
[26] Hafz N A M, Lee S K, Jeong T M and Lee J 2011 *Nucl. Instrum. Methods Phys. Res.* A **637** S51
[27] Walker P A *et al* 2013 *New J. Phys.* **15** 045024
[28] Manahan G G *et al* 2014 *New J. Phys.* **16** 103006
[29] Lundh O, Rechatin C, Lim J, Malka V and Faure J 2013 *Phys. Rev. Lett.* **110** 065005
[30] Kneip S *et al* 2009 *Phys. Rev. Lett.* **103** 035002
[31] Kneip S *et al* 2011 *Plasma Phys. Control. Fusion* **53** 014008
[32] Froula D H *et al* 2009 *Phys. Rev. Lett.* **103** 215006
[33] Ralph J E *et al* 2010 *Phys. Plasmas* **17** 056709
[34] Kalmykov S Y, Beck A, Yi S A, Khudik V N, Downer M C, Lefebvre E, Shadwick B A and Umstadter D P 2011 *Phys. Plasmas* **18** 056704
[35] Ta Phuoc K, Rousse A, Pittman M, Rousseau J P, Malka V, Fritzler S, Umstadter D and Hulin D 2003 *Phys. Rev. Lett.* **91** 195001
[36] Schwoerer H, Liesfeld B, Schlenvoigt H-P, Amthor K-U and Sauerbrey R 2006 *Phys. Rev. Lett.* **96** 014802
[37] Ta Phuoc K, Corde S, Thaury C, Malka V, Tafzi A, Goddet J P, Shah R C, Sebban S and Rousse A 2012 *Nat. Photon.* **6** 308
[38] Miura E, Ishii S, Tanaka K, Kuroda R and Toyokawa H 2014 *Appl. Phys. Express* **7** 046701
[39] Tsai H-E *et al* 2015 *Phys. Plasmas* **22** 023106
[40] Khrennikov K, Wenz J, Buck A, Xu J, Heigoldt M, Veisz L and Karsch S 2015 *Phys. Rev. Lett.* **114** 195003
[41] Chen S *et al* 2013 *Phys. Rev. Lett.* **110** 155003
[42] Powers N D, Ghebregziabher I A, Golovin G, Liu C, Chen S, Banerjee S, Zhang J and Umstadter D P 2014 *Nat. Photon.* **8** 28
[43] Sarri G *et al* 2014 *Phys. Rev. Lett.* **113** 224801
[44] Liu C, Golovin G, Chen S, Zhang J, Zhao B, Haden D, Banerjee S, Silano J, Karwowski H and Umstadter D P 2014 *Opt. Lett.* **39** 4132
[45] Shaw J M *et al* 2017 *AIP Conf. Proc.* **1812** 100012
[46] Lu W, Tzoufras M, Joshi C, Tsung F S, Mori W B, Vieira J, Fonseca R A and Silva L O 2007 *Phys. Rev. Accel. Beams* **10** 061301
[47] Fattahi H *et al* 2014 *Optica* **1** 45
[48] Haefner C L *et al* 2017 *Proc. SPIE* **10241** 1024102
[49] Corde S, Ta Phuoc K, Lambert G, Fitour R, Malka V and Rousse A 2013 *Rev. Mod. Phys.* **85** 1
[50] Kalmykov S Y, Beck A, Davoine X, Lefebvre E and Shadwick B A 2012 *New J. Phys.* **14** 033025
[51] Mora P and Antonsen T M Jr 1996 *Phys. Rev.* E **53** R2068
[52] Pukhov A and Meyer-ter-Vehn J 2002 *Appl. Phys.* B **74** 355
[53] Thomas A G R *et al* 2008 *Phys. Rev. Lett.* **100** 255002
[54] Tzoufras M, Tsung F S, Mori W B and Sahai A A 2014 *Phys. Rev. Lett.* **113** 245001
[55] Kalmykov S Y, Davoine X, Lehe R, Lifschitz A F and Shadwick B A 2015 *Phys. Plasmas* **22** 056701
[56] Cianchi A, Anania M P, Bisesto F, Castellano M, Chiadroni E, Pompili R and Shpakov V 2016 *Nucl. Instrum. Methods Phys. Res.* A **829** 343
[57] Krafft G A and Priebe G 2010 *Rev. Accel. Sci. Technol.* **3** 147
[58] He Z-H, Hou B, Nees J A, Easter J H, Faure J, Krushelnick K and Thomas A G R 2013 *New J. Phys.* **15** 053016
[59] He Z-H, Hou B, Lebailly V, Nees J A, Krushelnick K and Thomas A G R 2015 *Nat. Commun.* **6** 7156
[60] Lifschitz A F, Davoine X, Lefebvre E, Faure J, Rechatin C and Malka V 2009 *J. Comput. Phys.* **228** 1803
[61] Cowan B M *et al* 2012 *J. Plasma Phys.* **78** 469

[62] Lehe R, Lifschitz A F, Thaury C, Malka V and Davoine X 2013 *Phys. Rev. Accel. Beams* **16** 021301
[63] Decker C D, Mori W B, Tzeng K C and Katsouleas T 1996 *Phys. Plasmas* **3** 2047
[64] Jackson J D 1998 *Classical Electrodynamics* (New York: Wiley) p 676
[65] Mora P and Antonsen T M Jr 1997 *Phys. Plasmas* **4** 217
[66] Tzoufras M, Lu W, Tsung F S, Huang C, Mori W B, Katsouleas T, Vieira J, Fonseca R A and Silva L O 2009 *Phys. Plasmas* **16** 056705
[67] Benedetti C, Schroeder C B, Esarey E and Leemans W P 2014 *Phys. Plasmas* **21** 056706
[68] Grigsby F B, Dong P and Downer M C 2008 *J. Opt. Soc. Am.* B **25** 346
[69] Sanders J C, Zgadzaj R and Downer M C 2012 *AIP Conf. Proc.* **1507** 882
[70] Vicario C, Shalaby M, Konyashchenko A, Losev L and Hauri C P 2016 *Opt. Lett.* **41** 4719
[71] Wen M, Shen B, Zhang X, Ji L, Wang W, Xu J and Yu Y 2010 *Phys. Plasmas* **17** 103113
[72] Ma Y *et al* 2015 *Phys. Plasmas* **22** 083102
[73] Popp A *et al* 2010 *Phys. Rev. Lett.* **105** 215001
[74] Gizzi L A *et al* 2013 *Appl. Sci.* **3** 559
[75] Wiggins S M *et al* 2010 *Plasma Phys. Control. Fusion* **52** 124032
[76] Weingartner R *et al* 2011 *Phys. Rev. Spec. Top. Accel. Beams* **14** 052801